AGU PUBLICATIONS

JGR

Journal of Geophysical Research: Space Physics

RESEARCH ARTICLE
10.1002/2016JA023525

Special Section:
Major Results From the MAVEN Mission to Mars

Photochemical escape of oxygen from Mars: First results from MAVEN in situ data

Robert J. Lillis[1], Justin Deighan[2], Jane L. Fox[3], Stephen W. Bougher[4], Yuni Lee[4], Michael R. Combi[4], Thomas E. Cravens[5], Ali Rahmati[1], Paul R. Mahaffy[6], Mehdi Benna[6], Meredith K. Elrod[6], James P. McFadden[1], Robert. E. Ergun[2], Laila Andersson[2], Christopher M. Fowler[2], Bruce M. Jakosky[2], Ed Thiemann[2], Frank Eparvier[2], Jasper S. Halekas[7], François Leblanc[8], and Jean-Yves Chaufray[8]

[1]Space Sciences Laboratory, University of California, Berkeley, California, USA, [2]Laboratory for Atmospheric and Space Physics, University of Colorado Boulder, Boulder, Colorado, USA, [3]Department of Physics, Wright State University, Dayton, Ohio, USA, [4]Department of Climate and Space Sciences and Engineering, University of Michigan, Ann Arbor, Michigan, USA, [5]Department of Physics and Astronomy, University of Kansas, Lawrence, Kansas, USA, [6]NASA Goddard Space Flight Center, Greenbelt, Maryland, USA, [7]Department of Physics and Astronomy, University of Iowa, Iowa city, Iowa, USA, [8]LATMOS/CNRS, Université Pierre et Marie Curie, Paris, France

Key Points:
- Photochemical O escape fluxes from dissociative recombination of O_2^+ are calculated from MAVEN in situ data
- Escape rates of 1.2 to 5.5×10^{25} s^{-1} are derived and depend on season, solar zenith angle, and EUV flux, consistent with previous models
- We find a power law exponent of 2.6 for the EUV dependence of escape rate, implying 100 s of mbar of oxygen loss over 3.5 Gyr

Correspondence to:
R. J. Lillis,
rlillis@SSL.Berkeley.edu

Citation:
Lillis, R. J., et al. (2017), Photochemical escape of oxygen from Mars: First results from MAVEN in situ data, *J. Geophys. Res. Space Physics*, *122*, 3815–3836, doi:10.1002/2016JA023525.

Received 26 SEP 2016
Accepted 18 FEB 2017
Accepted article online 21 FEB 2017
Published online 29 MAR 2017

Abstract Photochemical escape of atomic oxygen is thought to be one of the dominant channels for Martian atmospheric loss today and played a potentially major role in climate evolution. Mars Atmosphere and Volatile Evolution Mission (MAVEN) is the first mission capable of measuring, in situ, the relevant quantities necessary to calculate photochemical escape fluxes. We utilize 18 months of data from three MAVEN instruments: Langmuir Probe and Waves, Neutral Gas and Ion Mass Spectrometer, and SupraThermal And Thermal Ion Composition. From these data, we calculate altitude profiles of the production rate of hot oxygen atoms from the dissociative recombination of O_2^+ and the probability that such atoms will escape the Mars atmosphere. From this, we determine escape fluxes for 815 periapsis passes. Derived average dayside hot O escape rates range from 1.2 to 5.5×10^{25} s^{-1}, depending on season and EUV flux, consistent with several pre-MAVEN predictions and in broad agreement with estimates made with other MAVEN measurements. Hot O escape fluxes do not vary significantly with dayside solar zenith angle or crustal magnetic field strength but depend on CO_2 photoionization frequency with a power law whose exponent is 2.6 ± 0.6, an unexpectedly high value which may be partially due to seasonal and geographic sampling. From this dependence and historical EUV measurements over 70 years, we estimate a modern-era average escape rate of 4.3×10^{25} s^{-1}. Extrapolating this dependence to early solar system, EUV conditions gives total losses of 13, 49, 189, and 483 mbar of oxygen over 1–3 and 3.5 Gyr, respectively, with uncertainties significantly increasing with time in the past.

1. Introduction

Photochemical escape in planetary atmospheres is a process by which (a) an exothermic chemical reaction produces an upward-traveling neutral particle whose velocity exceeds the planetary escape velocity and (b) the particle is not prevented from escaping through any subsequent collisions with thermal neutrals. At Mars, photochemical escape is thought to be the dominant loss process for neutrals heavier than hydrogen today [*Lammer et al.*, 2008], likely several times larger than heavy ion escape and thus one of the major pathways for atmospheric escape over the history of Mars. The photochemical escape of O, N, and C atoms is the result of photodissociation, photodissociative ionization, and electron-impact dissociative ionization of the primary neutral constituents primary CO_2, CO, N_2, O, and O_2, as well as dissociative recombination (DR) of the ion species N_2^+, CO^+, NO^+, and O_2^+ [*Fox and Hać*, 2009]. By approximately 2 orders of magnitude, the dominant escaping atom is O [cf. *Brain et al.*, 2017, Table 3], mostly the result of DR of O_2^+, the process upon which we will focus on in this study.

The critical altitude region for photochemical escape is within a few scale heights of the exobase (i.e., 170–250 km), i.e., the region sufficiently low in altitude that substantial amounts of O_2^+ are created, but where the mean free path is sufficiently large that energized hot O atoms can escape the atmosphere in substantial numbers without first losing too much energy through collisions.

Several numerical models of photochemical escape of O from Mars have been developed in recent years by using input from the two vertical profiles recorded by the Viking Landers [*Hanson et al*., 1976; *Nier et al*., 1976] and global circulation models [*Bougher et al*., 1999, 2000; *Gonzalez-Galindo et al*., 2013]. Photochemical escape rates range from 1.0 to $6.0 \times 10^{25}\,s^{-1}$ for equinox solar minimum conditions and from 4.0 to $22.0 \times 10^{25}\,s^{-1}$ for equinox solar maximum conditions, with an average of 2.75 for the ratio between the former and latter conditions [*Chaufray et al*., 2007; *Cipriani et al*., 2007; *Fox and Hac*, 2014; *Fox and Hać*, 2009; *Groller et al*., 2014; *Hodges*, 2002; *Krestyanikova and Shematovich*, 2005; *Lee et al*., 2015b; *Valeille et al*., 2009a, 2009b].

In addition, remote observations of Mars' oxygen exosphere from the Mars Atmosphere and Volatile Evolution Mission (MAVEN) mission have provided photochemical escape rate estimates. *Rahmati et al*. [2017] showed that pickup oxygen ion distributions measured by the Solar Wind Ion Analyzer [*Halekas et al*., 2015] from solar moderate (December 2014) and solar minimum (December 2015) conditions are consistent with an oxygen exosphere structure which implies a modeled escape rate of $7 \times 10^{25}\,s^{-1}$. Also, *Lee et al*. [2015a] modeled the altitude profiles of 130.4 nm oxygen emission from the Martian exosphere for solar moderate, perihelion conditions (where the escape rate was $\sim 3.5 \times 10^{25}\,s^{-1}$), finding that the intensity was a factor of ~1.5–2 lower than that measured by the Imaging Ultraviolet Spectrometer [*Deighan et al*., 2015; *McClintock et al*., 2015] for the same period. Since this emission is optically thin, this is consistent with a modeled escape rate of $\sim 5.2–7 \times 10^{25}\,s^{-1}$ from O_2^+ dissociative recombination. Lastly, *Cravens et al*. [2016] conducted a simplified theoretical analysis of photochemical escape from DR of O_2^+ in the Mars atmosphere, concluding that, under simplified assumptions such as an isothermal CO_2-only atmosphere, photochemical escape rates should be proportional to solar EUV irradiance and inversely proportional to the collision cross section between hot O and CO_2.

In this paper we present the first estimates of photochemical escape fluxes of atomic oxygen calculated from in situ data collected in the Martian thermosphere and ionosphere by the MAVEN spacecraft [*Jakosky et al*., 2014]. Section 2 discusses the data used and the caveats therewith. Section 3 describes the method of calculating photochemical escape and provides an example. Section 4 describes the results, comparing derived photochemical escape fluxes with season, solar zenith angle, and EUV photoionization frequencies, as well as establishing a range of likely escape fluxes for the modern era going back to 1947 and, finally, extrapolation backward in time to escape rates and total oxygen loss over the last several billion years. Section 5 discusses comparisons with earlier modeling efforts, uncertainties, complementary MAVEN remote-sensing measurements, and the trade-off between the kind of hot neutral escape described in this paper versus the direct energization of molecular ions via electric fields. Section 6 discusses conclusions and future work.

2. Data Used in This Study

Although photochemical escape of O cannot be directly measured by MAVEN (no instrument currently exists to measure the velocities of hot neutral atoms in the appropriate energy range of <10 eV), all of the important quantities upon which it depends are measured in situ in the Mars upper atmosphere, typically on at least every other orbit. We use in situ data from three instruments collected below 400 km during 1662 orbits spanning 10 February 2015 to 31 July 2016. We obtain temperatures and densities of ambient electrons measured by the Langmuir Probe and Waves (LPW) experiment [*Andersson et al*., 2015; *Andrews et al*., 2015; *Ergun et al*., 2015; *Fowler et al*., 2015]. We also use temperatures of thermal O_2^+ ions measured by the SupraThermal And Thermal Ion Composition (STATIC) experiment [*McFadden et al*., 2015]. Finally, we use densities of thermal O_2^+ ions and the thermal neutral species CO_2, CO, N_2, and O measured by the Neutral Gas and Ion Mass Spectrometer (NGIMS) [*Mahaffy et al*., 2014]. Other measured neutral species make up less than 1% of the density at the relevant altitudes [*Mahaffy et al*., 2015].

Here we describe a number of data selection and preparation issues. First, we choose to use only data from the inbound portion of each periapsis pass because reactive neutral species build up in the NGIMS instrument during periapsis, meaning that the background count rate is substantially lower for inbound compared to outbound passes. Second, due to imperfectly subtracted backgrounds above ~280 km, we replace all atomic oxygen density data above 280 km with an exponential function and a single scale

Table 1. The Four Non-Negligible Branches of the O_2^+ Dissociative Recombination Reaction and Their Likelihoods (i.e., Branching Ratios)

Initial State	Final State	Likelihood
$O_2^+ + e \rightarrow$	$O(^3P) + O(^3P) + 6.99$ eV	26.5%
	$O(^1D) + O(^3P) + 5.02$ eV	47.3%
	$O(^1D) + O(^1D) + 3.06$ eV	20.4%
	$O(^1D) + O(^1S) + 0.83$ eV	5.8%

height equal to the average scale height measured between 220 km and 280 km. It is important to note that this extrapolation has a negligible effect on derived escape fluxes because more than 90% of the escape flux originates below 280 km. Third, both NGIMS and STATIC measure thermal ion densities, but we choose to use NGIMS as the sole source of O_2^+ densities in this study due to an ongoing and as-yet-unresolved issue of low-energy ion suppression in STATIC. Note that, due to its very narrow field of view, NGIMS is optimized for measuring the kind of isotropic particle distributions we see in the photochemically dominated ionosphere; at higher altitudes, above ~300 km ions can be quite directional, and therefore, NGIMS underestimates ion densities. However, the vast majority of escaping ions are produced below 250 km, so this underestimation should not significantly affect the results. Fourth, we only use passes where a reliable electron temperature is derived by LPW at all altitudes. Fifth, we note that NGIMS cannot measure both ions and reactive neutral species (i.e., CO and O) on the same periapsis pass due to the need to warm up the filament that is used to ionize neutrals coming into the open source aperture [*Mahaffy et al.*, 2014]. For this reason, we use different subsets of the 1662 orbits to calculate dissociative recombination rates and escape probabilities, according to the availability of the relevant data in each set of orbits, as described in the next section. We will also compare derived escape fluxes with relevant parameters such as Mars season, crustal magnetic field strength, solar zenith angle, and CO_2 photoionization rate (see Appendix A).

3. Method for Calculating Photochemical Escape of Oxygen

In order to determine photochemical escape fluxes of hot oxygen from in situ measurements, we must separately calculate two different quantities as a function of altitude z: (1) the production rate of hot oxygen atoms from O_2^+ DR and (2) the probability that, once produced, a hot O atom will escape the atmosphere. The hot O production rate R, in number per cubic centimeter per second, is given by twice the DR rate (each reaction produces two oppositely directed O atoms):

$$R_{\text{hot O}}(z) = 2n_e(z)n_{O_2^+}(z)k(T_e(z)) \quad (1)$$

where $n_{O_2^+}(z)$ and $n_e(z)$ are the densities of the ambient thermal O_2^+ ions and electron, respectively, and k is the DR rate coefficient. The DR cross section depends primarily on electron velocity, and thus, the rate coefficient k depends on electron temperature, with a dependence best fit by the following expression [e.g., *Petrignani et al.*, 2005]:

$$k = 1.95 \times 10^{-7} \left(\frac{300}{T_e}\right)^{0.70} \text{cm}^3\text{s}^{-1} \quad (2)$$

The probability of escape for an O atom produced by DR depends on two main factors: the initial energy of the atom and the column density and composition of the gas above the altitude where it was "born." DR occurs via four main channels, with the resulting O atoms each leaving

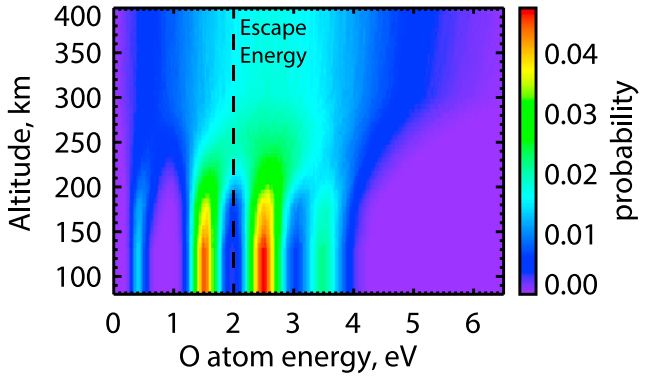

Figure 1. Example probability distribution of hot O atom energies as a function of altitude. The escape energy (at 200 km altitude) of 1.98 eV is shown with a dashed black vertical line.

Table 2. Cross Sections for Oxygen Collisions With Neutral Species Used in the Hot O Transport Calculations

Collision Process	Cross Section	Reference
O strikes CO_2	2.0×10^{-14} cm^2	[*Fox and Hac*, 2014]
O strikes O	0.6×10^{-14} cm^2	[*Kharchenko et al.*, 2000]
O strikes N_2	1.8×10^{-14} cm^2	[*Balakrishnan et al.*, 1998]
O strikes CO	1.8×10^{-14} cm^2	Assume same as N_2 above

with half of the exothermic energy in the center of mass frame of the electron-ion collision. The four channels are given in Table 1 with their relative likelihoods [*Fox and Haćć*, 2009].

The upper two of these reactions result in individual O energies in excess of the escape energy (at 200 km altitude) of 1.98 eV. The final energies of the resulting O atoms in the atmospheric rest frame depend on the relative velocities of the electrons and O_2^+ ions and hence on electron and ion temperature. We note that this dependence on ionospheric plasma temperatures is small, since such temperatures are typically <0.1 eV [*Ergun et al.*, 2015] at the altitudes (~180–250 km) from which most photochemical escape occurs, but we include them for completeness. Therefore, the energy distribution of nascent hot oxygen atoms (and the fraction of those with energies above the escape energy) varies with altitude, from close to 4 delta functions (with the energies shown above) at lower thermospheric altitudes to a somewhat broader distribution in the exosphere. An example of the altitude-energy distribution of hot O atoms is shown in Figure 1.

For each set of neutral density and electron and ion temperature profiles, we run a three-dimensional Monte Carlo hot atom transport model to calculate escape probabilities as a function of altitude. We assume that the atmosphere is spherically symmetric with the same altitude profile everywhere. Hot O atoms start at a set altitude and are given random directions and an initial energy drawn at random from the initial energy distribution for that altitude (mentioned in the previous paragraph). They are propagated through collisions with thermal neutrals, using the cross sections shown in Table 2. Angular-dependent cross sections are assumed to be the same for all species and are taken from *Kharchenko et al.* [2000]. We run this model at each altitude until 2500 hot oxygen atoms escape (i.e., reach the top of the simulation with escape energy or greater). Two thousand five hundred divided by the number of atoms spawned gives the escape probability. Starting from 400 km, we work down in altitude until the escape probability falls below 5×10^{-5}.

Once we have calculated the altitude profiles of the hot O production rate and the hot O escape probability, we simply multiply these two quantities together at each altitude step to get the production rate of

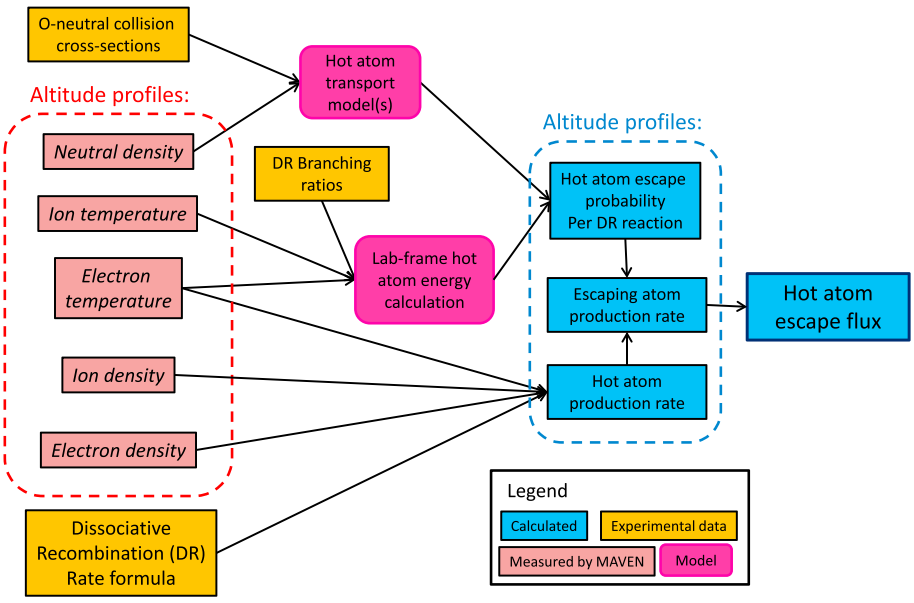

Figure 2. Flowchart explaining calculation of hot oxygen escape from measured altitude profiles of neutral densities and ion and electron densities and temperatures.

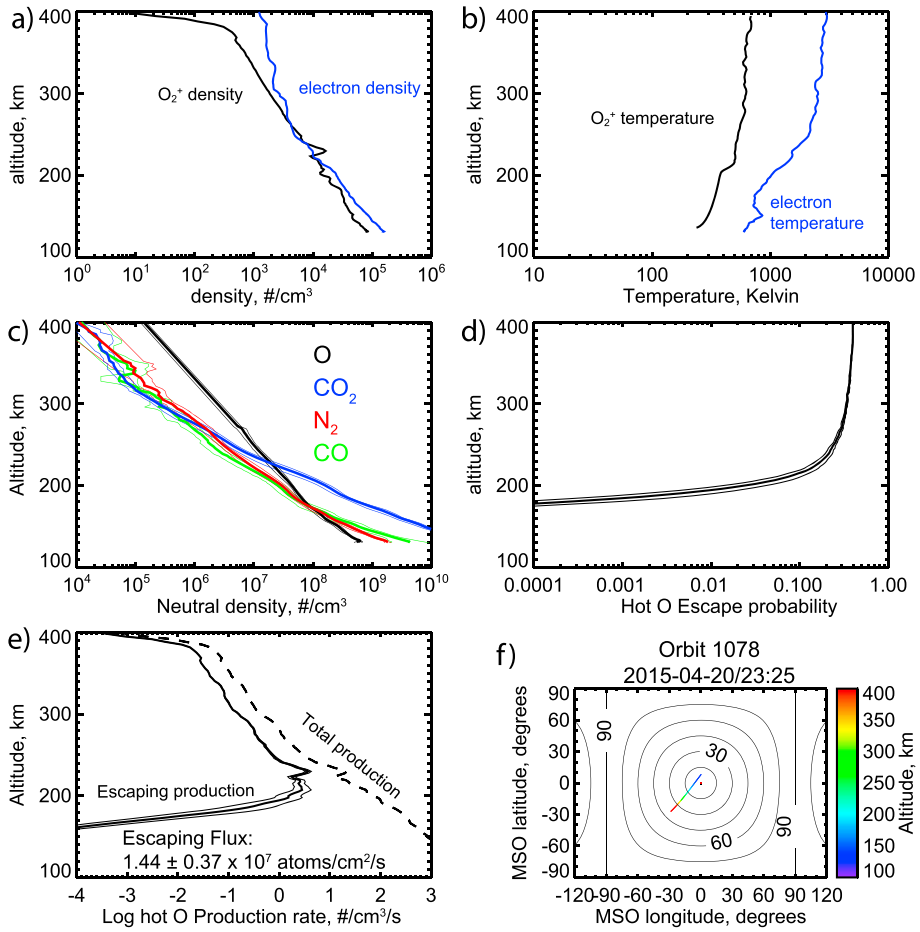

Figure 3. Example of escaping flux calculation for orbit 1078, on 20 April 2015. Altitude profiles of measured and calculated quantities (see Figure 2 for how they relate): (a) electron density (from LPW) and O_2^+ density (from NGIMS); (b) electron temperature (from LPW) and O_2^+ temperature (from STATIC); (c) neutral density profiles measured by NGIMS on the previous and subsequent orbits (thin lines) and the averages of those (thick lines); (d) escape probabilities for hot O atoms calculated by using the neutral densities from the previous and subsequent orbits (thin lines) and their averages (thick line); (e) production rate of hot O atoms from the dissociative recombination of O_2^+, where the dashed line shows total production and the solid lines show just the production rate of escaping atoms (thick line and thin lines correspond to those in Figure 3d). Integrating these lines with respect to altitude gives the total escaping flux and its uncertainty, shown within Figure 3e. (f) MAVEN's trajectory during this time in MSO coordinates, where the 15° increments in solar zenith angle are shown with contours.

escaping hot O. We then integrate with respect to altitude to get the hot O escape flux for that particular periapsis pass. Figure 2 is a flowchart of this calculation, relating the quantities measured by MAVEN, formulae derived from experiment, models, and calculated values.

As mentioned in section 2, the profiles of all necessary quantities shown in the left magenta boxes in Figure 2 are not measured in the same orbit. Therefore, for each of the 815 orbits where we are able to determine the hot oxygen production rate profile (i.e., where full profiles of electron temperature, electron density, and O_2^+ density are measured; see the lower blue box in Figure 2), we multiply by an escape probability profile (upper blue box in Figure 2) that is the mean of the escape probability profiles determined (from the neutral density, ion temperature, and electron temperature) measured on the previous and subsequent orbits. An example calculation is shown in Figure 3 for a periapsis in April 2015, during MAVEN's second "deep dip" campaign in the vicinity of the subsolar point, when the periapsis altitude was ~130 km. The derived escape flux of $\sim 1.4 \times 10^7$ O atoms per square centimeter per second is fairly typical of the dayside during the data collection period, as discussed in the next section.

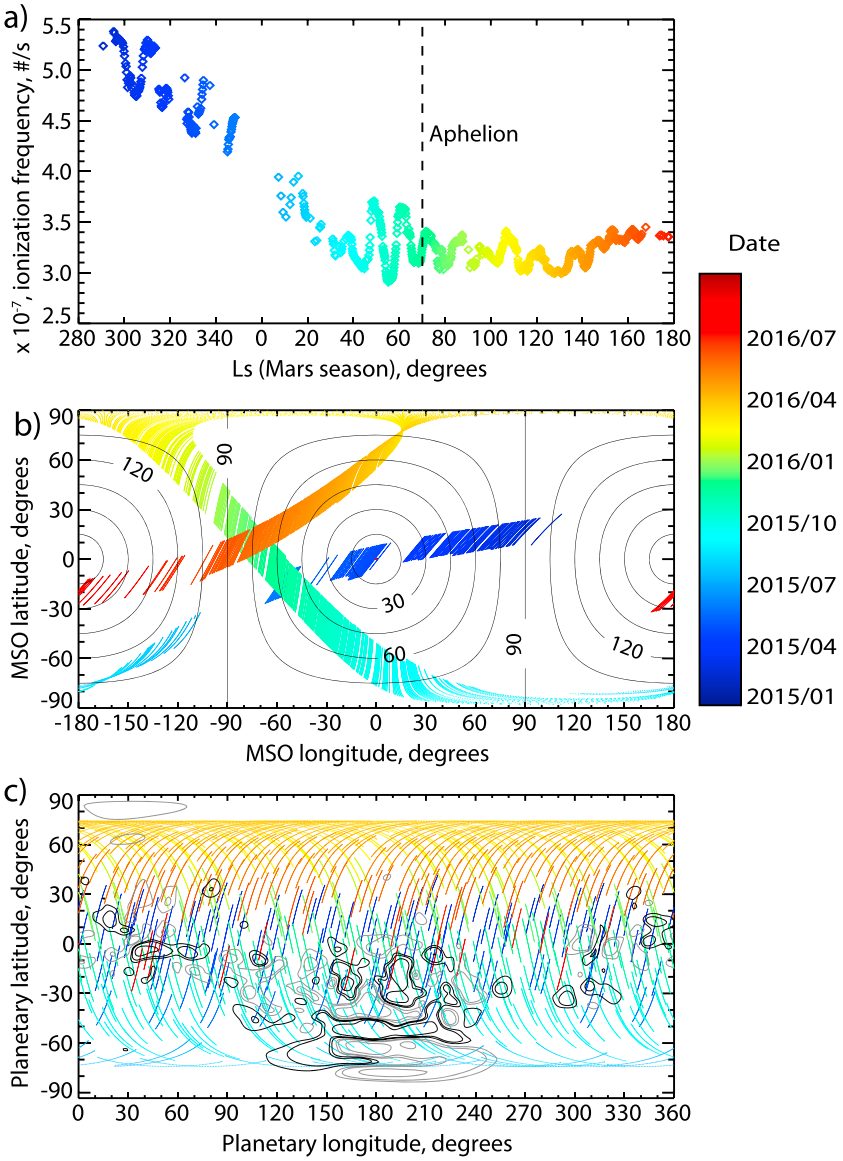

Figure 4. Data coverage for this study. All three panels are colored by date, covering from 10 February 2015 to 31 July 2016. (a) CO_2 photoionization frequency (see Appendix A) versus Mars season (Mars year 32 and 33). (b) The locations of all data taken below 250 km altitude, in MSO coordinates (15° increments of solar zenith angle are shown with contour lines) and planetary coordinates, respectively. (c) The positive (black) and negative (gray) contours of crustal magnetic field at 400 km altitude at ±10, 20, 50, and 100 nT.

Note that this calculation assumes that the measured profiles are precisely vertical, when in fact the spacecraft travels ~2000 km laterally during each inbound pass below 500 km. However, the vast majority (>90%) of the total escape originates between ~180 and 280 km, during which time the spacecraft moves ~750 km. Indeed, *Lillis et al.* [2015] reported <10% differences in simulated hot O escape fluxes calculated by using radial versus along-track profiles through the Mars Thermospheric Global Circulation Model [*Bougher et al.*, 1999, 2000].

We also calculated uncertainty for each derived value of escape flux. This is done by propagating the published uncertainties in the electron density, O_2^+ density, and electron temperature through calculating the altitude profile of uncertainties in the production rate of hot O. This is then convolved with the uncertainty in the escape probability profile, which is simply taken to be half the difference between the probability profiles calculated by using the neutral densities measured on the previous and subsequent orbits. The result is the uncertainty in the altitude profile of the production of escaping hot O. We then propagate this

uncertainty through each step of the integration with respect to altitude to arrive at an uncertainty in each escape flux measurement. These are typically several tens of percent and are shown in Figure 7a.

4. Results

4.1. Data Coverage

Figure 4 shows coverage for all data used in this study. Figure 4a shows how the total CO_2 photoionization frequency at Mars (see Appendix A) decreases by up to 45% with time as Mars moving further from the Sun toward and past aphelion. The short-term variations are due to solar rotation as active regions on the Sun's surface rotate in and out of view of Mars. Figures 4b and 4c show the spacecraft location below 250 km in Mars solar orbital (MSO) coordinates and planetary coordinates, respectively. The data set begins at the dusk terminator, which continues across the subsolar point and continues out to about 60° solar zenith angle on the dawn side during a period of relatively high solar EUV irradiance. There are a substantial number of profiles in this timeframe (particularly between 20° and 45°) which suffered from unreliable electron temperature profiles due to large negative spacecraft potentials and so are unusable. There is also a data gap coinciding with solar conjunction and other technical problems with NGIMS for all of June 2015. July and August 2015 are on the nightside in the southern hemisphere. Periapsis then crosses the dayside from southern hemisphere dusk in September 2015 to northern hemisphere dawn in January 2016 for aphelion atmospheric and EUV conditions. It then continues into the northern hemisphere nightside, before crossing back into daylight from the North Pole in February 2016 and crossing the dawn terminator once more in May 2016 and continuing toward the antisolar point in northern spring. The geographic coverage is broad in longitude as expected as the planet rotates underneath MAVEN's orbit.

4.2. Escape Fluxes

4.2.1. Broad Trends

All 815 derived values of the escape flux of O atoms from DR of O_2^+ are shown in Figures 5 and 6. Figure 5 shows that escape fluxes are substantially higher in early 2015, when Mars is comparatively close to the Sun and the Sun is reasonably active (approximately solar moderate conditions), ranging from 4 to $8 \times 10^7/cm^2/s$. As Mars recedes and solar activity diminishes, photoionization frequency drops and average escape fluxes drop correspondingly during the same period. By the time MAVEN's periapsis is on the dayside again in October 2015, ionization frequencies have dropped by ~40% from their highest values and derived escape fluxes have dropped by a factor of two or more. From then until mid-2016, both ionization frequencies and dayside escape fluxes stay generally low.

In addition, there are some interesting features beyond this general trend positive dependence on EUV flux. The first is that photochemical escape is reasonably constant with respect to solar zenith angle over the parts of the dayside MAVEN sampled and where full profiles were available. This is seen clearly in Figure 5 but particularly in Figures 6a and 6b. However, beyond ~100° solar zenith angle, we see a very wide range in escape fluxes, varying by more than 3 orders of magnitude. This is somewhat to be expected, given the highly variable and inhomogeneous nature of the Mars nightside ionosphere, which is due to strong temporal and geographic variabilities in electron precipitation and hence ionization [e.g., *Lillis et al.*, 2011; *Němec et al.*, 2011].

The second pattern is that we see an apparent dawn-dusk asymmetry in escape fluxes. Figure 5b and particularly Figure 6b show that escape fluxes are typically higher on the duskside than the dawn side, with the difference increasing with solar zenith angle. However, dawn and dusk, both sampled twice during the dates in question, were sampled at different seasons and latitudes. Therefore, while such an asymmetry is physically plausible (ions can survive for some time after sunset but have not yet been produced before sunrise, and cross-terminator flow seems to favor duskside [*Benna et al.*, 2015]), confirmation of a dawn-dusk asymmetry in photochemical escape awaits more sampling.

Figure 6c shows that, within this limited data set, there is no statistically significant correlation between crustal magnetic field strength and derived photochemical escape fluxes, either on the dayside or nightside. Note, however, that this comparison would only reveal the broadest trends, since the fluxes are classified according to the magnitude of the crustal magnetic field at 400 km at the latitude and longitude of the

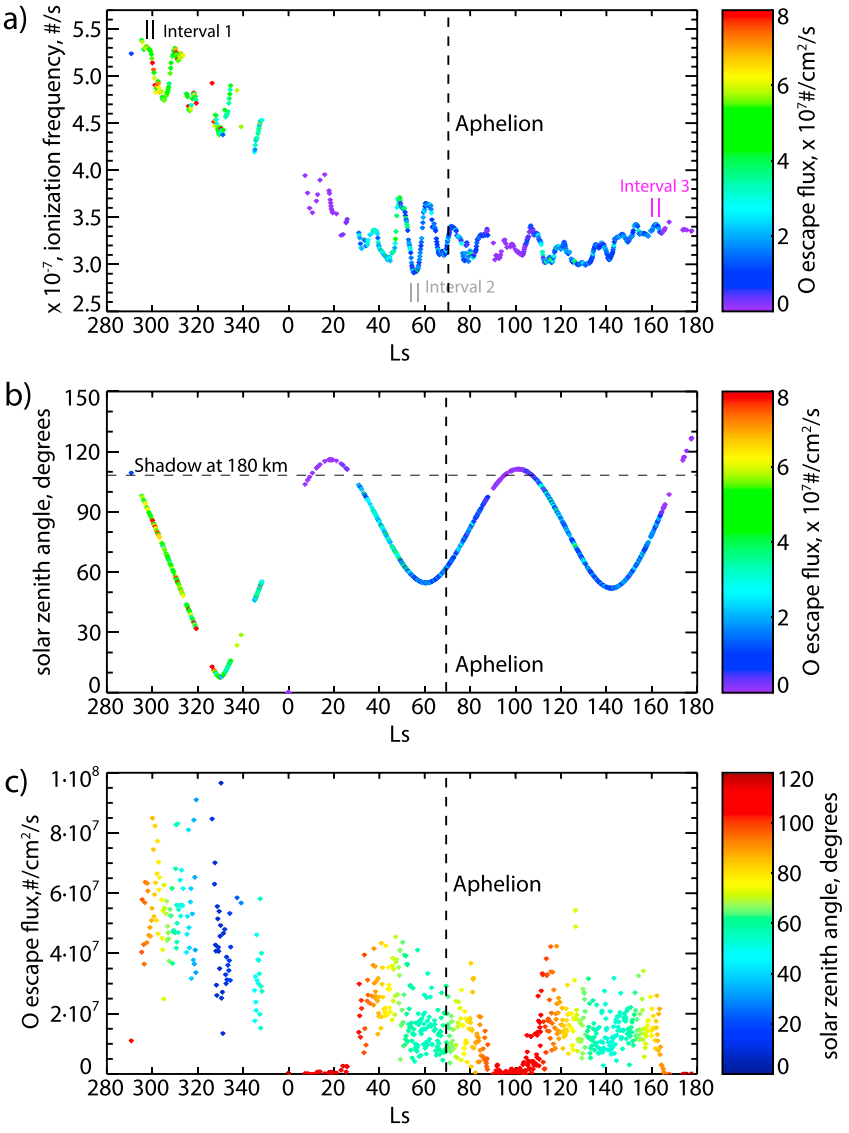

Figure 5. Derived O escape fluxes from DR of O_2^+. (a and b) Escape fluxes by color as a function of Mars season (*x* axis) with EUV ionization frequency (see Appendix A) and solar zenith angle on the *y* axis, respectively. (c) O escape fluxes as a function of Mars season (*x* axis) and solar zenith angle (colors). The vertical bars in Figure 5a refer to the three intervals listed in Table 3 and discussed in section 4.3.

periapsis. A more detailed study (left to future work) would examine the specific magnetic topology and magnitude at each individual point where the production rate of escaping hot O is calculated.

4.2.2. Short-Term Variability

Factors of ~2–3 variability within a short time span are not unusual. This "statistical" variability arises both natural variability in the physical system and our sampling of that system. Let us first discuss natural variability. First, although variations in total neutral mass density should not affect escape fluxes (because the ionospheric profile should simply move up and down in response), relative changes in the densities of different neutral species will affect escape fluxes in two different ways: (a) CO_2 is the main source for the O_2^+ ions that dissociatively recombine [*Schunk and Nagy*, 2000] and (b) different species have different cross sections for collisions with hot O atoms that are produced from the recombination. Such relative density changes between species are caused by tides and gravity waves in the Martian thermosphere and are not only expected [e.g., *Medvedev and Yigit*, 2012] but have been observed in data from both the Imaging Ultraviolet Spectrometer (IUVS) and NGIMS [*England et al.*, 2016]. Second, the dayside ionosphere can be quite "lumpy" due to ion transport near and above the exobase along crustal magnetic field lines, as was

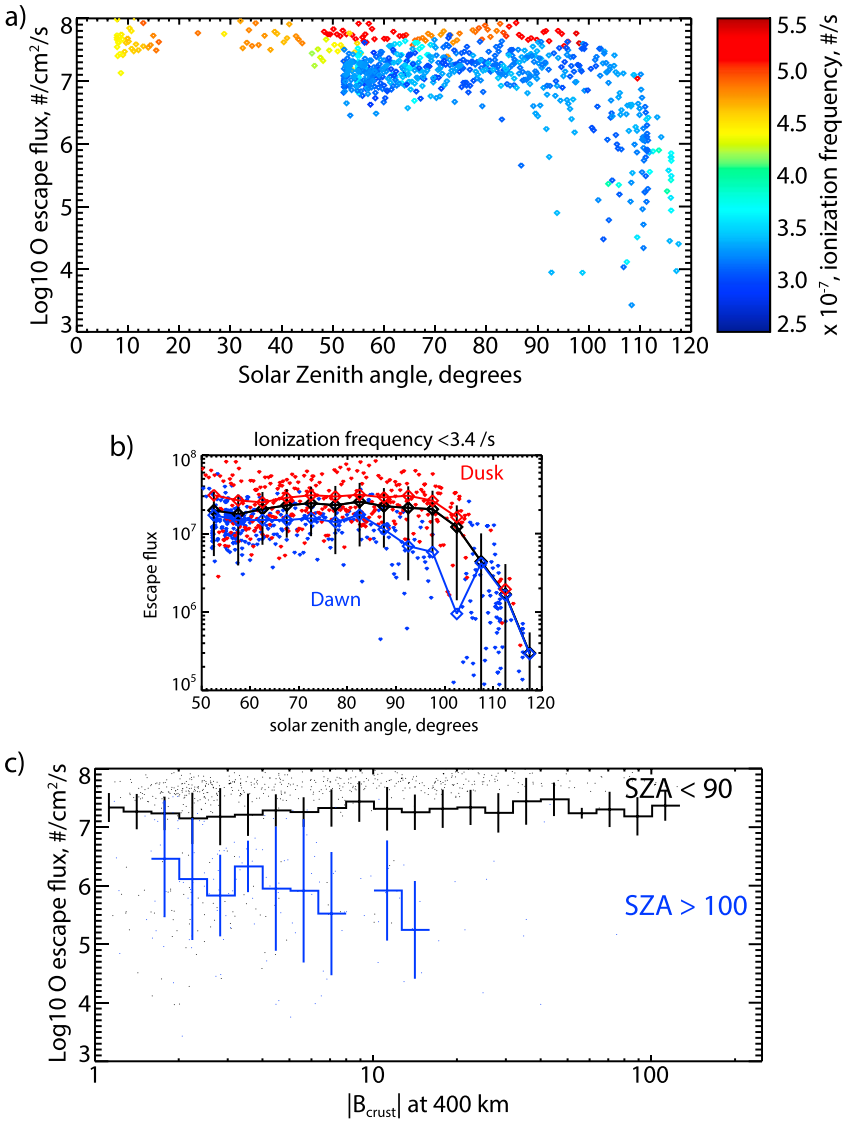

Figure 6. Derived O escape fluxes from DR of O_2^+. (a) O escape fluxes as a function of solar zenith angle at periapsis (*x* axis) and photoionization frequency (see Appendix A) (colors). (b) Escape fluxes vary with solar zenith angle for low ionization frequency values ($<3.4\ s^{-1}$) separately for dawn (blue) and dusk (red) sides of the planet. The small diamonds are individual escape flux measurements, while the large black diamonds are binned averages. (c) O escape fluxes and their standard deviations binned by the crustal magnetic field strength from the low-noise crustal magnetic field model of *Morschhauser et al.* [2014] evaluated at 400 km altitude above the periapsis location, with dayside periapses shown in black and nightside in blue.

observed in radar echoes from the Mars Advanced Radar for Subsurface and Ionosphere Sounding instrument on Mars Express [*Morgan et al.*, 2008]. Third, despite being a minor contributor to total ionization on the dayside, impact ionization from precipitating electrons and ions tends to peak at higher altitudes (160–200 km) [*Lillis et al.*, 2011, 2008] than photoionization (~130 km) [e.g., *Hanson et al.*, 1977] and thus can play a proportionally larger role in determining O_2^+ densities at the altitudes from which escape is occurring. This precipitation is temporarily highly variable and therefore can also contribute to variability [*Lillis and Brain*, 2013]. Fourth, currents in the dayside ionosphere, driven by neutral winds, electric fields, and magnetic gradient/curvature drifts, can drive local variability in both electron and ion densities [*Fillingim et al.*, 2012; *Riousset et al.*, 2013].

In addition, part of the statistical variability we see is due to uncertainty in our input profiles. Uncertainties in electron and ion densities are typically several tens of percent [*Benna et al.*, 2015; *Ergun et al.*, 2015]. Also, more

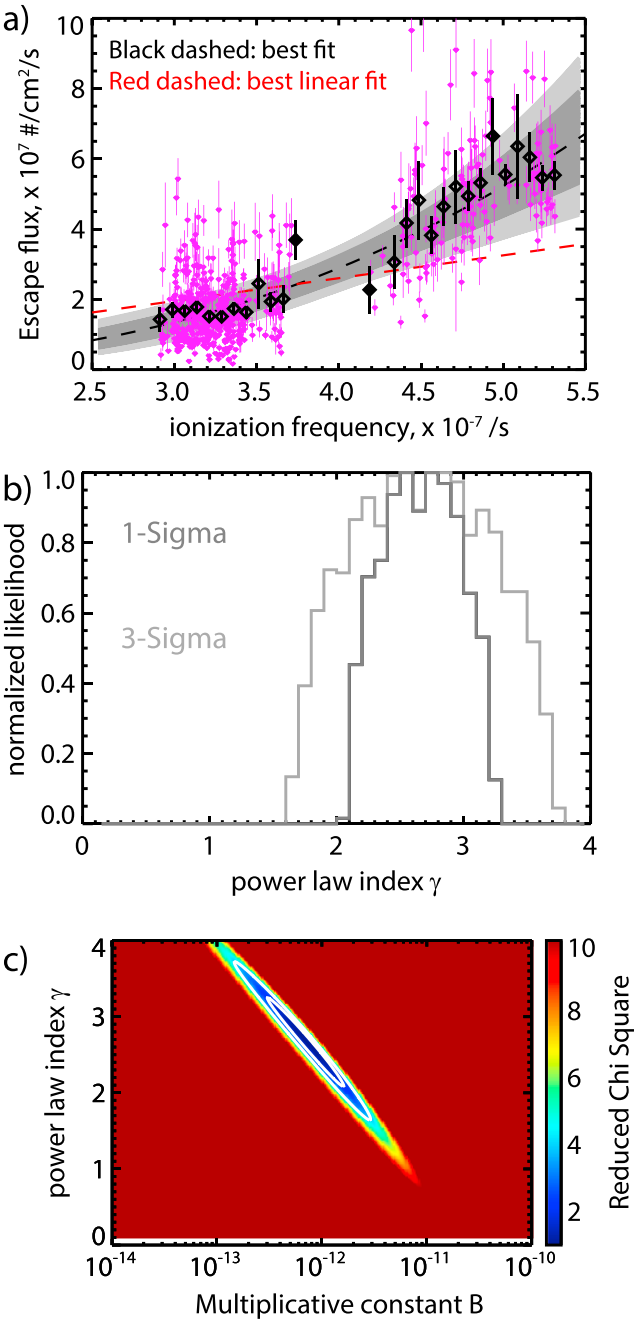

Figure 7. Dependence of dayside O escape fluxes on CO_2 photoionization frequency. (a) All 594 individual dayside (SZA < 95°) derived escape flux values (small pink dots with error bars) and binned values (black diamonds) with standard errors (standard deviations divided by the square of the number of samples) in each bin. All power law fits to these binned averages that fall within the 1σ and 3σ error ellipsoid are shown as dark and light gray lines, respectively. The best fit (power law index of 2.64) is shown in black. A dashed red line shows the best linear fit that goes through the origin. (b) A histogram of the power law indices for each fit that lies within the 1σ (dark gray) and 3σ (light gray) error ellipsoids. (c) The chi-square surface for these fits as a function of the power law index and the constant term, with the white contour that is drawn for 1σ and 3σ error ellipsoids. The reduced chi-square minimum is ~1.1, which is consistent with a model appropriately fitting the data and uncertainties being estimated appropriately.

importantly, the escape probability profile varies exponentially with altitude and is calculated by assuming the average of the neutral densities measured on the previous and subsequent orbits; factors of 2–3 orbit-to-orbit variability are not unusual in the Mars thermosphere [e.g., *Keating et al.*, 1998] and so could also plausibly account for this variability.

4.2.3. Correlation With Solar EUV Irradiance

Next we examine the variability in escape fluxes due to changing EUV irradiance. We choose to use CO_2 photoionization frequency instead of irradiance because it more directly determines the rate of production of molecular oxygen ions (see Appendix A for details), which leads to photochemical escape when they dissociatively recombine. This relationship between ionization frequency and photochemical escape is especially important because the early Sun was substantially brighter in the EUV [*Ribas et al.*, 2005] (see section 4.5). Figure 7a shows all 594 of the derived values of O escape flux taken with solar zenith angles less than 95° (i.e., dayside) as a function of the photoionization frequency, along with binned averages and standard errors (standard deviations divided by the square of the number of samples). We fit this distribution with the function:

$$F_{escape} = BI^{\gamma} \quad (3)$$

where F_{escape} is the derived escape flux in #/cm^2/s, I is the measured ionization frequency in s^{-1}, and B and γ are fitting parameters. We did not add a constant term to the right-hand side of equation (3) because solar EUV is by far the dominant source of ionization in the Martian atmosphere and because test fits resulted in a consistently negative constant term, which is unphysical in the context of photochemical escape.

Reduced chi-square values were calculated by using the average and

standard error for every bin (black symbols in Figure 7). All fits within the 1σ and 3σ error ellipsoids are shown in dark and light gray, respectively, and a histogram of power law indices for those fits is shown in Figure 7b. The full two-dimensional chi-square space is shown in Figure 7c. The best fit exponent is 2.64 but with a moderate spread within 1σ. This is unexpectedly high, as we discuss below.

4.2.4. An Unexpected Relationship to Solar EUV Irradiance

In general, EUV irradiance should be the main variable factor for the three primary quantities for determining photochemical escape: (a) photoionization rates, which determine electron and ion densities; (b) electron temperatures, which determine recombination rates (these two directly determine the production rate of hot O atoms; see equation (1)); and (c) thermospheric/exospheric neutral temperatures, which affect hot O transport [e.g., *Zhao and Tian*, 2015]. In a theoretical examination of photochemical escape of O, *Cravens et al*. [2016] show that, under a set of simplifying assumptions including an isothermal CO_2 atmosphere and a single EUV wavelength, photochemical escape flux should depend linearly on solar EUV irradiance only and no other variable factor. However, as the dashed red line in Figure 7a shows, the best fit linear function does not fit the derived escape fluxes very well. What explanations may there be for the much higher best fit power law exponent of ~2.6?

Here it is appropriate to distinguish between non-EUV factors potentially affecting escape fluxes that are expected to vary with Mars season and factors that are expected to vary with solar activity alongside EUV irradiance. The effects of these should ideally be quantified and separated and their effects removed from the comparison with solar EUV flux. The former could then be removed from any long-term extrapolation to past, higher EUV levels, while the latter could be included as a separate dependence on heliospheric conditions such as solar wind velocity, density, and magnetic field. Such a separation and quantification is beyond the scope of this paper. Nonetheless, it is useful to discuss these non-EUV factors.

Let us first address the seasonally varying factors, wherein it is important to reiterate that we are not deriving global photochemical escape rates in this study but local escape fluxes in discrete swaths of the atmosphere. Our periapsis measurements are taken along a single "track" in latitude, solar zenith angle, and Mars season as MAVEN's orbit precesses in time (see Figure 4). Therefore, any conclusions we may draw about the dependence of escape flux on EUV irradiance are subject to the assumption that all the sources of short-term variability discussed in the previous subsection "wash out" over seasonal time scales and across latitudes and solar zenith angles: gravity waves and tides, ion transport, charged particle impact ionization, and ionospheric currents. However, of these, Martian gravity waves are known to be stronger in the southern hemisphere in southern spring and summer near perihelion [*Wright*, 2012] and rates of charged particle precipitation are known to be higher when solar wind pressure is higher [*Lillis and Brain*, 2013], as it is when Mars is closer to the Sun near perihelion. As mentioned, we shall not attempt to quantitatively assess what these impacts may be, but they may serve to enhance the positive correlation between hot O escape fluxes and photoionization frequency we see in Figure 7, since all of the high EUV measurements (ionization frequency $> 4.5 \times 10^{-7}\,s^{-1}$) were taken in southern summer and early autumn.

Next we address those factors which are expected to vary with solar activity alongside EUV. Ion transport, ionospheric currents, and charged particle precipitation (both ionization and heating of neutrals) may all reasonably be expected to increase near the exobase with increased heliospheric activity. The former two may have a positive or negative effect on ion densities in different geographic regions or overall, while impact ionization from charged particles should increase hot O production. In other words, it is difficult to assess to what degree these factors, all of which should roughly correlate with solar EUV, may be contributing to a higher best fit power law in Figure 7. Even if we could separate these effects from those of EUV, a further complication is that, unlike solar EUV irradiance [*Ribas et al*., 2005], the historical record of solar wind speed and density and frequency and intensity of heliospheric disturbances is quite uncertain, due primarily to uncertainty in early solar rotation rates [e.g., *Johnstone et al*., 2015]. Nonetheless, in this study, we will use the range of functional forms of EUV dependence shown in Figure 7 in our extrapolations to both modern-day (section 4.4) and ancient (section 4.5) conditions.

4.3. Understanding Variability in Escape Fluxes

Let us now turn attention to the root causes of higher or lower derived photochemical escape fluxes in terms of the atmospheric and ionospheric conditions that determine those fluxes. As explained in

Table 3. The Dates, Prevailing Conditions, and Derived O Escape Fluxes (and Standard Deviations) for Each of the Three Intervals

Interval	1 (Black)	2 (Gray)	3 (Pink)
Dates	25 February 2015 to 1 March 2015	13 October 2015 to 19 October 2015	29 May 2016 to 3 June 2016
Ls	297°–301°	54°–57°	160°–163°
IAU latitude	31°–34°N	34°–39°S	38°–42°N
MSO latitude	22°–24°N	48°–55°S	13°–17°N
SZA	85° to 92°	56° to 59°	78° to 86°
Local time	16.7–17.1	11.2–11.8	6.0–6.5
Ionization frequency, 10^{-7} #/s	5.26 ± 0.06	2.94 ± 0.04	3.40 ± 0.02
O escape flux ($\times 10^7$ /cm^2/s)	5.4 ± 1.3	1.2 ± 0.8	1.4 ± 0.5

section 3, the photochemical escape flux at a given altitude depends not only on the plasma density there but also on the total column of neutral density above that altitude and its composition, as well as on electron temperature (which determines the recombination rate coefficient). In order to gain a clearer picture of the origin of the variability we see in Figures 5–7, let us examine the profiles of these important determining factors of escape flux for three representative time intervals. These intervals were chosen for their combination of season, solar zenith angle, and EUV irradiance to illustrate how the profiles of different quantities determine the escape flux. They are shown in Table 3 and Figure 5a. Interval 1 (black) is near the dusk terminator just after perihelion during the highest period of EUV irradiance observed by MAVEN (although not historically high; see Figure 10) so far. Interval 2 (pink) is near noon at midsouthern latitudes at the very lowest EUV flux observed just before aphelion, and interval 3 (gray) is near the dawn terminator near the equator for a somewhat higher EUV irradiance typical of most of 2016. Recall that the ion and electron temperatures do not have a significant impact on the energy distribution of the newly created hot O atoms, but the electron temperature is important in that it determines the rate of their creation (see section 3).

First we note that the markedly higher electron and ion densities (Figures 8a and 8b) seen for interval 1 (black) are most of the reason why the production rate of hot O is much higher than that for the other intervals, although the slightly lower recombination rate (Figure 8d) due to lower electron temperature (Figure 8c) plays a minor role too. However, we also note that the bulk of the escaping hot O atoms originates from a higher altitude because the lower atmosphere is warmest near perihelion, and therefore, the exobase mass density is higher (Figure 8e), pushing both the ionosphere and the escape region 25 km higher than interval 3 and ~15 km higher than interval 2 (Figure 8f).

Also, we notice that the peak and total production rate of escaping atoms is higher during interval 3 (pink) than during interval 2 (gray). This is due to higher EUV irradiance causing higher peak plasma densities. We also notice that the escaping atoms originate from a lower altitude because the lower Mars atmosphere is cooler (i.e., lower densities at the homopause) near dawn at 40° north latitude in northern spring for interval 2 than at noon at ~35° south latitude in southern winter for interval 3.

Figure 9 is an attempt to show intuitively that the reason for the different photochemical escape fluxes during these intervals lies in the different paths they take through the parameter space defined by the production of hot O (mostly determined by plasma density) and the retardation of its escape by collisions with thermal neutrals (mostly O and CO_2). Figure 9a shows binned averages of the production rate of escaping hot O atoms as a function of column mass density (on an inverted scale so that its logarithm is a proxy for altitude) and O_2^+ density. The contours show that there is a "sweet spot" in altitude for the production of escaping hot O, where the plasma density is high enough to cause a large O production rate but the column density above is sufficiently low that the O can escape. Also shown are the paths taken by the average values of these quantities for the three intervals. It is important to note that the total escape flux is the integral of the production rate of escaping O, with respect to altitude, along this path. Thus, it is clear (as it is from Figure 8f) that interval 1 has a higher escape flux than interval 2 because its average altitude profile traverses a higher plasma density with respect to the same range of column mass densities. Figure 9b shows the binned production rate of escaping O atoms with respect to O_2^+ density, and electron temperature, limited to a narrow range of column mass

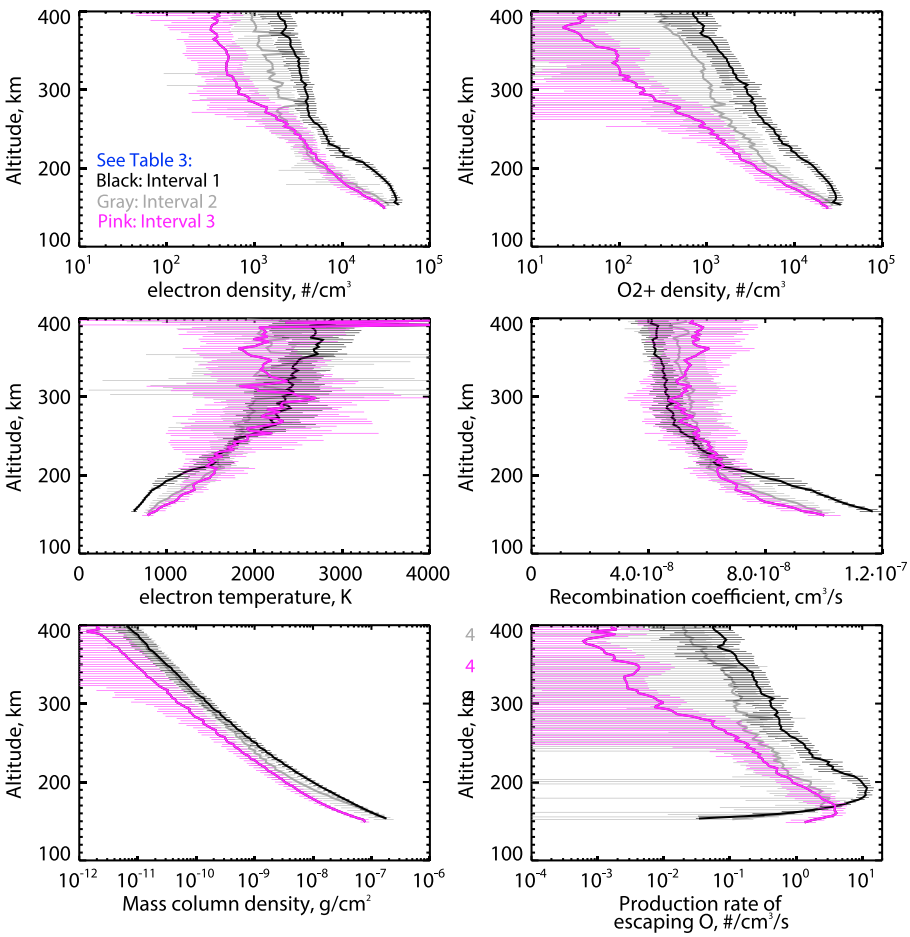

Figure 8. Examination of three particular intervals in the data set (details in Table 3 and Figure 5). Intervals 1–3 are denoted by black, gray, and pink, respectively. All panels show means and standard deviations, as a function of altitude: (a) electron density, (b) O_2^+ ion density,(c) electron temperature, (d) dissociative recombination rate coefficient (which depends only on electron temperature),(e) mass column density above each altitude, and (f) production rate of escaping hot O atoms.

densities (0.5 to 1.5×10^{-8} g/cm^2) showing the comparatively modest, but non-negligible, effect of electron temperature on escape fluxes.

4.4. Estimates of Global Escape Rates in the Present-Day Epoch

Given that there is no discernible trend in escape fluxes with solar zenith angle on the dayside (see Figure 6), it is reasonable to simply multiply our escape fluxes by the area of the dayside of Mars up to 103° solar zenith angle SZA: $2.45\ \pi\ (R_{\mathrm{Mars}} + 200\ \mathrm{km})^2 = 9.92 \times 10^{17}\ \mathrm{cm}^2$, where R_{Mars} is the area-weighted average radius of the Martian areoid (3389.9 km). Given the range of altitudes over which the production of escaping O occurs, it is reasonable to use a convenient area of 10^{18} cm^2, by which we can multiply all escape flux numbers in order to get global escape rates.

One of the prime goals of the MAVEN mission is to constrain the total loss of atmosphere over Martian history. In order to build a baseline from which we may extrapolate photochemical O escape rates backward in time, we must estimate the average escape rate over the modern epoch, i.e., over the range of solar EUV irradiance conditions that exist in the modern era. The results are shown in Figure 10, where Figure 10a shows the weekly photoionization frequency (calculated as described in Appendix A) since 1947 on the basis of direct measurements back to 2002, satellite measurements of solar Lyman alpha irradiance back to 1978, and ground-based measurements of F10.7 solar radio flux prior to 1978 [*Thiemann et al.*, 2017]. Figure 10b

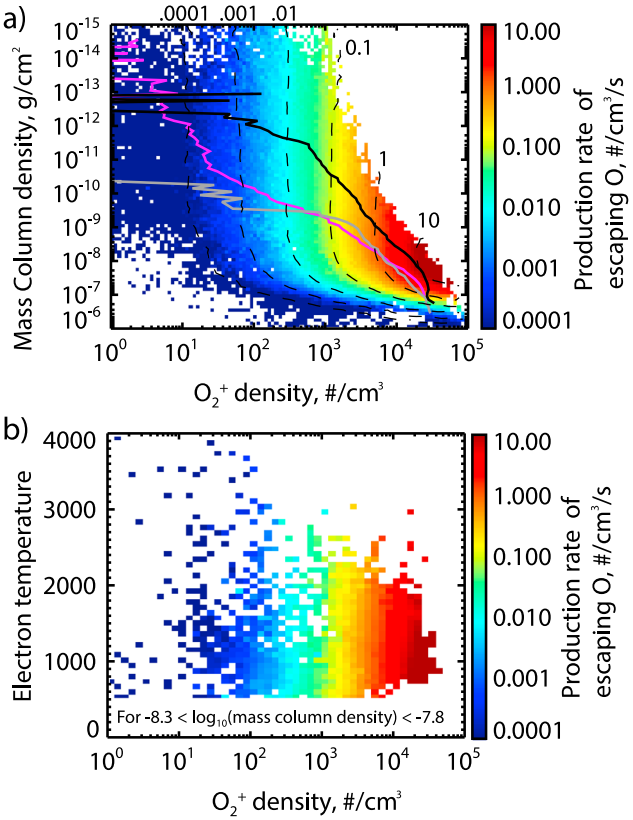

Figure 9. (a) Binned averages of the production rate of escaping hot O atoms as a function of column mass density (on an inverted scale so that its logarithm is a proxy for altitude) and O_2^+ density. Superimposed are the paths taken through this two-dimensional parameter space for the averages of each of the three intervals, using the same colors used in Figure 8 and Table 3. Note that the total escape flux is the integral (with respect to altitude) along such paths. (b) Binned averages of the production rate of escaping hot O atoms as a function of electron temperature and O_2^+ density for a narrow range of column mass density (0.5 to 1.6×10^{-8} g/cm^2), showing the relatively moderate effect of electron temperature.

shows the range of escape rates over the same time that are consistent with the power law indices within the 1σ χ^2 error ellipsoid of fits to the EUV dependence of derived escape rates shown in Figure 7. Figure 10c shows a histogram of every escape rate data point shown in Figure 10b. Although there are a few points (for larger power law indices, perihelion, and solar maximum) over the decades where rates can reach 4×10^{26} s^{-1}, 80% of the values lie within the range of 1.1 to 9.1×10^{25} s^{-1}. With values that vary over such a large range, it is reasonable to characterize the standard deviations in terms of logarithms, giving us a mean (lower bound and upper bound) of 4.3 (1.9, 9.6) $\times 10^{25}$ O atoms per second in the modern epoch.

4.5. Estimates of Historical Atmospheric Escape Rates and Loss

We now have in hand a modern-day estimate for photochemical escape rates and a range of dependences on EUV flux. This allows us to make estimates of escape rates at earlier times in solar system history. We are specifically concerned with the evolution of solar ultraviolet irradiance from ~10 to 89 nm, i.e., photons capable of ionizing CO_2 (see Figure A1c). Several studies have been carried out by using observations of G-type (i.e., Sun-like) stars, each fitting the observed decrease in irradiance with the functional form $t^{-\beta}$, where t is the stellar age in billions of years. *Ayres* [1997] found that β is approximately 1 for the ionization of H, O, O_2, and N_2 specifically. *Ribas et al.* [2005] used six stars with a range of ages from 0.1 to 6.7 Gyr and found β values of 1.20 and 1.23 for the wavelength ranges 10–36 and 0.1–110 nm, respectively. *Tu et al.* [2015] combined a stellar rotational evolution model with observations of hundreds of stars in young stellar clusters and found $\beta = 1.22$ for 10–90 nm. Therefore, for this study, we will adopt $\beta = 1.2$ and leave to future work a more detailed analysis where β has rigorous uncertainties and wavelength dependence. Our expression for the time evolution of the ionization frequency I_{past} is thus

$$I_{past} = I_{present}\left(\frac{t_{past}}{4.5\ \mathrm{Gyr}}\right)^{-1.2} \quad (4)$$

where $I_{present}$ is the mean of the ionization frequency from the 70 year reconstructed record Flare Irradiance Spectral Model for Mars (FISM-M) shown in Figure 10a: 4.3×10^{-7} s^{-1}; t_{past} is the age of Mars at some point in the past in billions of years. The resulting estimate of ionization frequency over solar system history is shown in Figure 11a.

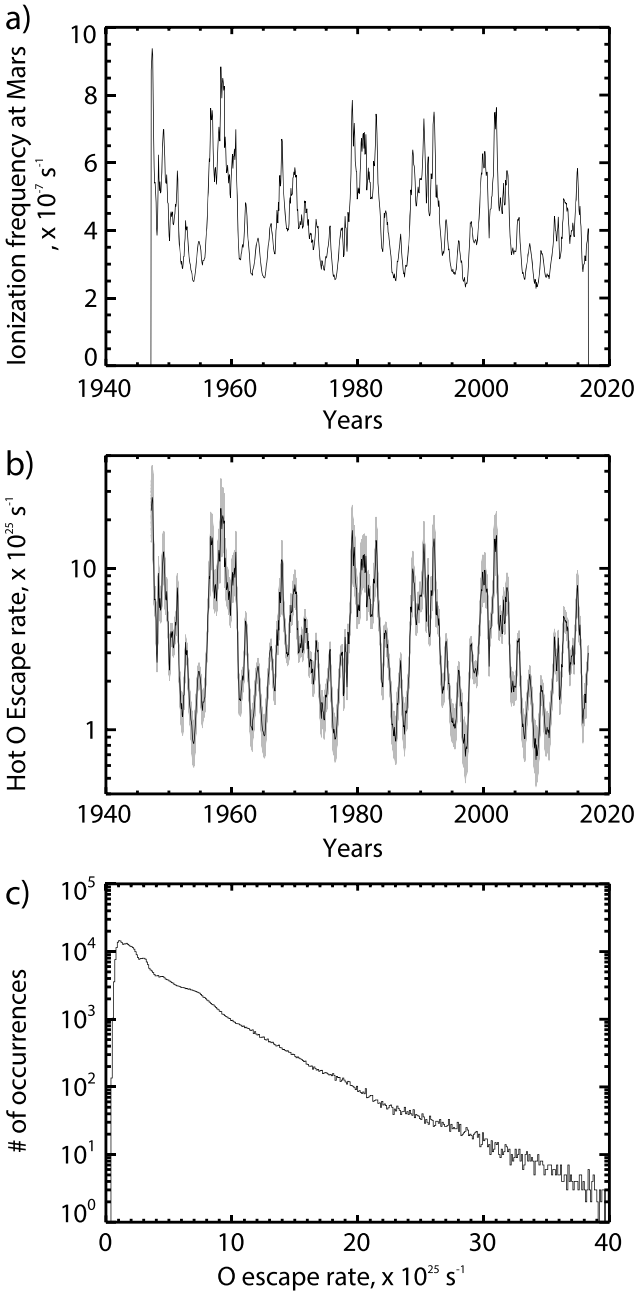

Figure 10. Estimate of photochemical escape fluxes in the modern era. (a) The weekly CO_2 photoionization frequency calculated at Mars using FISM-M since 1947 [*Thiemann et al.*, 2017]. (b) The range of escape rates over the same time that are consistent with the power law indices within the $1\sigma\ \chi^2$ error ellipsoid of fits to the photoionization frequency dependence of derived escape rates shown in Figure 7. (c) A histogram of every escape rate data point in Figure 10b.

We assume the modern-era mean of 4.3×10^{25} O atoms per second (see previous section) for the present-day escape rate $R_{present}$ and scale-up past escape rates R_{past} according to the power law dependence on ionization frequency from equation (3).

$$R_{past} = R_{present}\left(\frac{I_{past}}{I_{present}}\right)^{\gamma} = R_{present}\left(\frac{t_{past}}{4.5\ \mathrm{Gyr}}\right)^{-1.2\gamma} \quad (5)$$

Recasting in terms of billions of years ago:

$$R_{past} = R_{present}\left(\frac{4.5}{4.5 - t_{\mathrm{Gyr\ ago}}}\right)^{1.2\gamma} \quad (6)$$

We then use the best fit and 1σ range of power law indices derived in section 4.2 (and shown in Figure 7) to extrapolate O escape rates and cumulative loss back to 4.4 Gyr ago, shown in Figures 11b and 11c, respectively. For comparison, we also show the very simplistic and unrealistic case of simply extrapolating current escape rates back to the early solar system (blue dashed lines) and a linear EUV dependence from the theoretical result of *Cravens et al.* [2016] (red dashed lines). Table 4 gives the same information in tabular form, for 0–3, 3.5, and 4 Gyr ago, where the 10th and 90th percentiles shown are from the distribution of 1σ values of power law indices shown in Figure 7b. Figure 12 shows the shape of these distributions explicitly, both in terms of escape rates (Figure 12, left column) and cumulative loss (Figure 12, right column).

Figures 11 and 12 demonstrate clearly the importance of constraining the functional dependence of photochemical escape fluxes on ionization frequency (which is determined by solar EUV irradiance). For example, 6 times higher EUV at 3.5 Gyr ago leads to 6 times higher escape if the power law index 1 (i.e., linear dependence, per the theoretical model of *Cravens et al.* [2016]) but 53 times higher if the index is 2.2. Therefore, better constraining the EUV dependence of photochemical escape rates is a primary concern as more data are collected during MAVEN's extended mission.

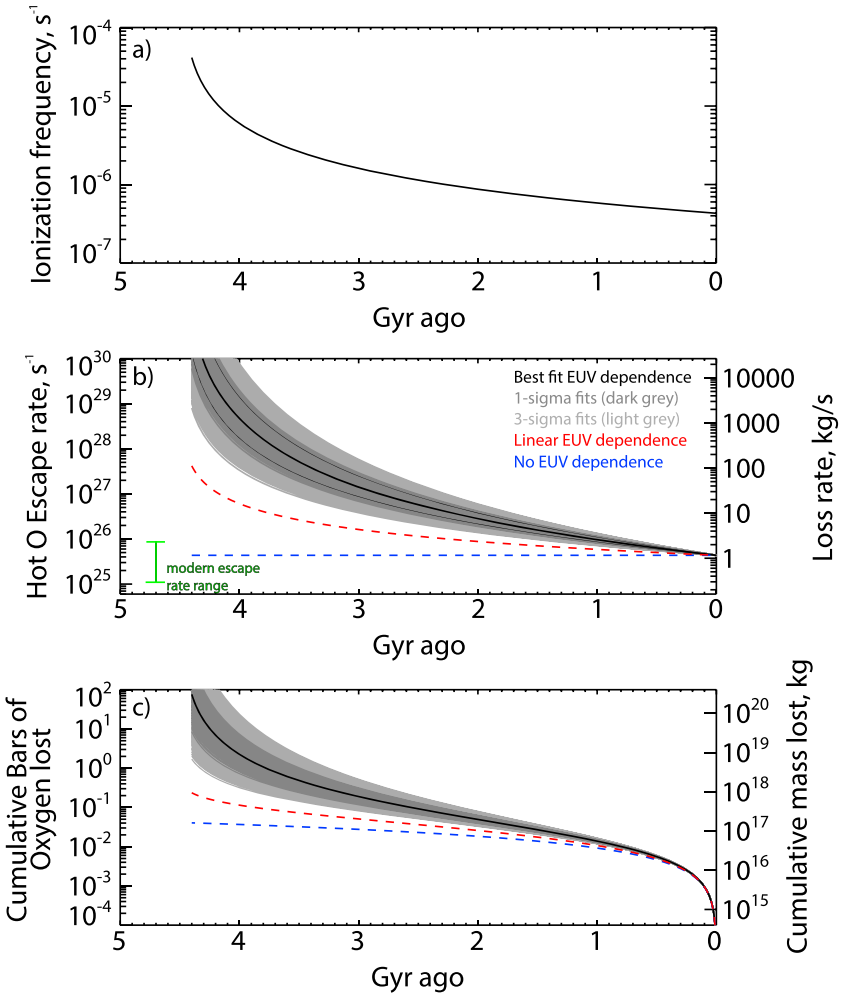

Figure 11. Extrapolation of photochemical O escape rates over Martian history. (a) The assumed history of CO_2 photoionization frequency irradiance, taken from *Ribas et al.* [2005]. (b and c) The resulting escape rates and cumulative oxygen lost, respectively, assuming the best power law fit (2.64) to photoionization frequency dependence (thick black), the range of 1σ power law fits shown in Figure 7 (gray), the 10th and 90th percentiles of those distributions (thin black), a linear dependence (red dashed) [*Cravens et al.*, 2016], and no EUV dependence, i.e., a simple extrapolation back in time of the present-day escape rate (blue dashed). The green vertical bar in Figure 11b shows the 1σ range of escape rates over the modern era.

Table 4. Extrapolation of Photochemical O Escape Rates From Dissociative Recombination of O_2^+ and Resulting Cumulative Loss of Oxygen Over Martian History

	Present	1 Gyr	2 Gyr	3 Gyr	3.5 Gyr	4 Gyr
Ionization frequency ($\times 10^{-7}$ s^{-1})	4.3	5.8	8.8	16	26	62
O escape rates $\times 10^{25}$ s^{-1}						
Best fit EUV dependence	4.3	9.7	28	146	534	4990
(10th and 90th percentiles of extrapolated escape rates)		(8.7, 11.1)	(22, 38)	(88, 253)	(270, 1140)	(1800, 15,000)
Linear EUV dependence	4.3	5.9	8.8	16	27	62
No EUV dependence	4.3	4.3	4.3	4.3	4.3	4.3
Total oxygen lost (mbar)						
Best fit EUV dependence	0	13.9	49.3	189	483	2250
(10th and 90th percentiles)	0	(13.0, 14.8)	(42, 59)	(136, 278)	(270, 850)	(1000, 5500)
Linear EUV dependence	0	10.7	25.8	51	73	114
No EUV dependence	0	9.2	18.4	27.6	32	37

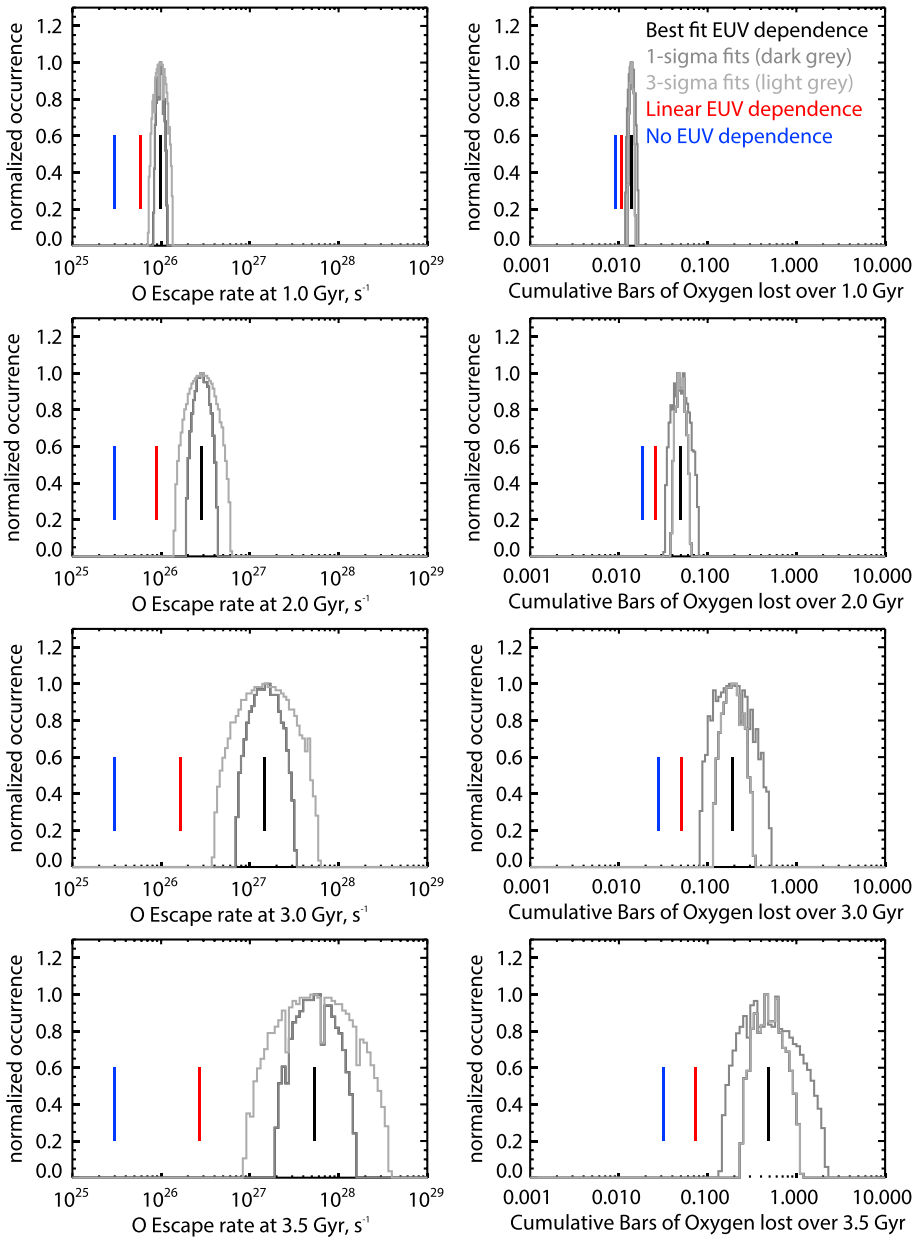

Figure 12. (left column) Probability distributions for escape rates and (right column) cumulative loss of oxygen over Martian history, with the first through fourth rows reflecting 1–3 and 3.5 Gyr ago, respectively. The vertical black, red, and blue lines reflect values of escape rates and cumulative losses for different assumptions of EUV dependence: best fit from Figure 7 (black), linear (red) [*Cravens et al.*, 2016], and none (blue).

There are three caveats to mention here. The first is that these extrapolations do not incorporate the variability in modern escape fluxes we have both observed in the MAVEN data set and inferred over the modern era (section 4.4); for reference, the inferred modern escape rate range is shown with a green vertical bar in Figure 11b. The second is that we have not assumed any uncertainty in the historical EUV flux, although some undoubtedly exist and may be significant. While the stellar irradiance-versus-age curves derived by *Ribas et al.* [2005] do not seem to have large error bars, the 10th, 50th, and 90th percentiles for the time-decay exponent β in young stellar clusters derived by *Tu et al.* [2015] are 0.96, 1.22, and 2.15. The upper end of this range would certainly make for substantially higher inferred escape fluxes at early times. The third and most important caveat is that we should not expect photochemical escape flux dependence on solar EUV to be constant throughout Martian history. While higher pressures in the past

Table 5. Solar Cycle Variability in Modeled Photochemical Escape Rates of Atomic Oxygen From Mars Compared With Calculated Escape Rates From This Study[a]

This Study	$L_S = 345°–348°$, Moderate Solar Activity, 46–55° SZA	
Lower bound, mean, upper bound	1.0, 2.0, 3.0	
Reference	$L_S = 0°$, low solar activity	$L_S = 0°$, high solar activity
Groller et al. [2014]	1.5	2.1
Fox and Hac [2014]eroded	0.94	1.9
Fox and Hac [2014]noneroded	1.8	4.3
Valeille et al. [2010]	3.8	13.5
Chaufray et al. [2007]	1.0	4.0
Cipriani et al. [2007] case A	0.55	2.6
Cipriani et al. [2007] case B	3.4	8.5
Krestyanikova and Shematovitch [2005]	4.5	
Hodges [2002]	4.4	18.0
Kim et al. [1998], corrected by *Nagy et al.* [2001]	3.4	8.5
Lee et al. [2015b]	1.4	3.1

[a]Rates are given in units of $10^{25}\ s^{-1}$.

should simply push the source of escape to higher altitudes, higher EUV in the past should increase thermospheric temperatures and lead to larger columns of atomic oxygen above the O_2^+-rich region, retarding escape. Indeed, *Zhao and Tian* [2015] show that, for this reason, photochemical escape of oxygen from the DR of O_2^+ is actually lower for 20 times current EUV than for 10 times current EUV. Moreover, the total relative amounts of relevant species N, C, H, and O in Mars' atmosphere should evolve over time, leading to different relative amounts of O_2^+ versus other ions near the exobase and hence a different escape picture.

5. Discussion

5.1. Comparison With Previous Models of Photochemical O Escape

Let us now compare these results with the models mentioned in the introduction, for which the two Viking Lander profiles and derived global models were the only input. These models assume northern spring equinox ($L_s = 0°$) and low- and high-solar activities and, typically, a solar zenith angle of 60°. Therefore, to ensure the most meaningful "apple-to-apple" comparison, let us compare these with escape rates derived between $L_s = 340°$ and 350°: $3.0 \pm 1.0 \times 10^{25}\ s^{-1}$. Given the weakness of the current solar cycle, our ionization frequency (4.3 to $4.5 \times 10^{-7}\ s^{-1}$) is slightly higher than what would be called "solar moderate." Table 5 compares our escape rates with modeled escape rates from several authors. Our rates fall within the range of several studies, in particular *Groller et al.* [2014], *Fox and Hac* [2014], *Chaufray et al.* [2007], *Cipriani et al.* [2007], and *Lee et al.* [2015b], whose low- and high-solar activity estimates bracket those from the present study.

5.2. Uncertainties and Comparison With MAVEN Remote Estimates of Photochemical Escape

It is useful to compare our derived photochemical escape rates with estimates that are consistent with remote MAVEN measurements of pickup oxygen ions [*Rahmati et al.*, 2017] ($\sim 7 \times 10^{25}\ s^{-1}$) and 130.4 nm oxygen emission [*Lee et al.*, 2015a] (5 to $7 \times 10^{25}\ s^{-1}$), which were mentioned in the introduction. Those measurements were taken in late 2014 near perihelion ($L_s = 250°$) when CO_2 ionization frequencies were 5.6 to $6.2 \times 10^{-7}\ s^{-1}$, i.e., 15–20% higher than our interval 1 for which our mean derived escape rate is $5.3 \times 10^{25}\ s^{-1}$ (see Table 3). Given all the sources of uncertainty, both instrumental and modeling, in the method of *Rahmati et al.* [2017] and *Lee et al.* [2015a], and the present study, this represents surprisingly good agreement between the methods.

However, likely more important than these sources of error, it is important to note the following caveats in our calculations of escape fluxes reported in this paper. The first is that there may still be as-yet undetermined systematic uncertainties in the quantities measured by NGIMS and LPW (although these data sets have

undergone multiple revisions as of January 2017). Since the study uses several different quantities, such systematic uncertainties may cancel one another out or may compound. The second, and potentially most important, is that the O–CO_2 collision cross section has not yet been measured in the laboratory and the value used here from *Fox and Hac* [2014], with the angular dependence from *Kharchenko et al*. [2000], could be in error by up to a factor of 2, leading to a similar systematic uncertainty in escape fluxes. However, the fact that we see relatively good agreement between this study and *Rahmati et al*. [2017] (which did not require cross sections) implies that the O–CO_2 cross section may not be in error by more than a few tens of percent. Lastly, we note that *Lee et al*. [2015a] modeled the coronal emission by using simulated (i.e., not measured) thermosphere and ionosphere and an O–CO_2 cross section 40% lower than the one used in this study. Therefore, we speculate that the relatively good agreement with this study may be due to these two factors partially canceling out.

5.3. Competition Between O_2^+ DR and Direct O_2^+ Escape

The altitude region within a few scale heights of the exobase (~170–250 km) is critical for understanding atmospheric escape from Mars in general. As shown in Figures 3e and 8f, this is the region sufficiently low in altitude that substantial amounts of O_2^+ are created but where the mean free path is sufficiently large that energized particles (neutrals or ions) can escape in substantial numbers without first thermalizing through collisions. O can be energized through the O_2^+ dissociative recombination (DR) reaction discussed in this paper, but both O^+ and O_2^+ created in this region can also be energized by an ambipolar electric field or by direct heating via plasma waves. *Ergun et al*. [2016] modeled these processes in 1-D, showing that, under extreme conditions, direct escape of O_2^+can result in a larger O loss than DR of O_2^+, in the following manner. First, high EUV fluxes can raise electron temperatures, which in turn raises the ambipolar electric field to the point where a thermal ion can be accelerated to escape velocity. Second, electromagnetic Poynting flux from the solar wind can directly heat these ions and provide them with escape velocity. Note that we need not model plasma processes in this work since we do not assume photochemical equilibrium in our calculations. However, these processes and the resulting energization and escape of O_2^+could be responsible for reducing O_2^+ densities above the exobase and hence for some of the variability we see in photochemical O escape fluxes.

6. Conclusions and Future Work

The study presented in this paper is the first effort to constrain, with the relevant in situ measurements, an important atmospheric loss channel for the Mars atmosphere: the escape of hot oxygen atoms from Mars via dissociative recombination of O_2^+ ions. The derived escape rates are consistent with some of the many previous modeling efforts on this topic and with estimates of escape rates derived from other MAVEN instruments [e.g., *Rahmati et al*., 2017]. However, the observed dependence of escape solar EUV irradiance is significantly stronger than the linear dependence expected from simplified models [*Cravens et al*., 2016]. The physical reasons for this observed dependence remain to be explained, including the relative impact of (a) seasonal influences such as gravity waves from the lower atmosphere and thermospheric winds, (b) plasma transport and currents in the ionosphere, and (c) ionizing effects of precipitation of magnetospheric plasma.

Our goal is ultimately to understand how photochemical escape varies spatially and with respect to season and solar influences. Models validated by reproducing this behavior can then be more confidently used to determine escape rates as we iteratively add atmosphere and increase solar EUV properties appropriately as we move backward in time, in order to gain a full picture of the importance of this escape process in the climatic evolution of Mars. Therefore, until we understand these influences and separate (insofar as possible) their causes into EUV-related and solar wind-related, extrapolations to past heliospheric conditions (as in section 4.5) will be quite uncertain beyond the uncertainties in those conditions themselves.

In the future, we intend to make simultaneous estimates of O escape rates, both from pickup O ions [*Larson et al*., 2015; *Rahmati et al*., 2015] and in situ thermospheric/ionospheric measurements (i.e., this work) in order to constrain the crucial O–CO_2 collision cross section. Such comparisons have not been possible due to orbit geometry but should be in late 2016.

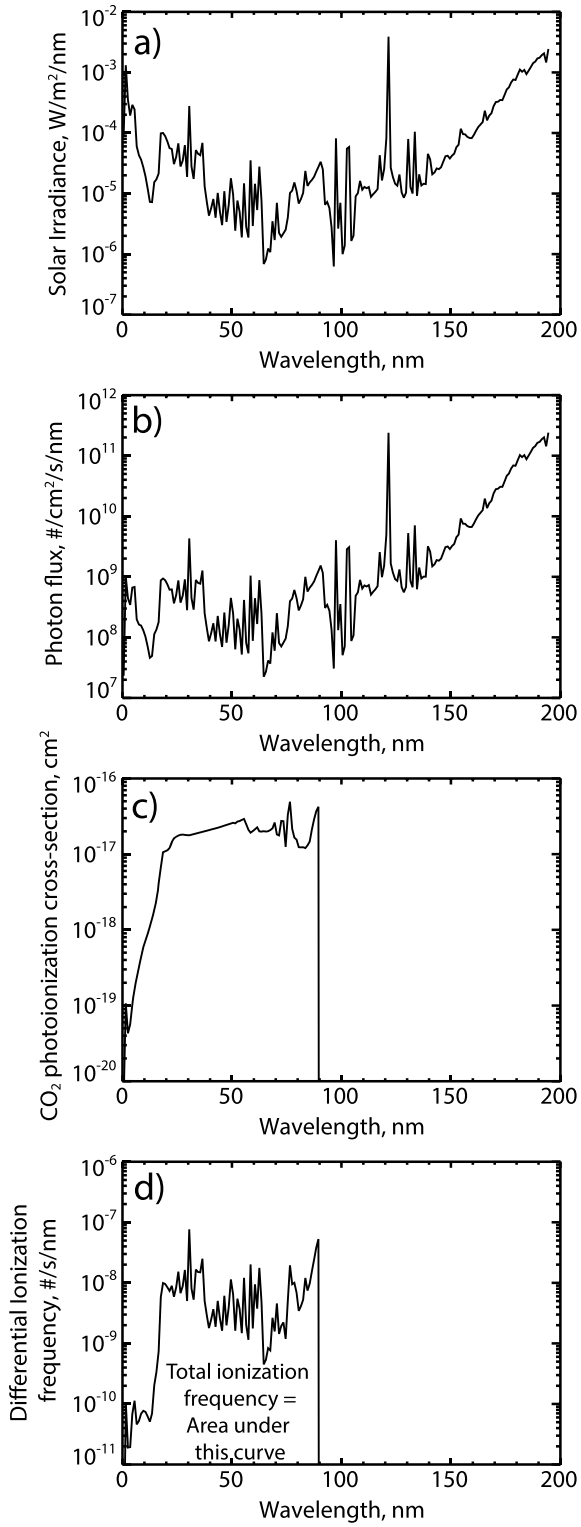

Figure A1. Calculation of total ionization frequency. All panels are shown as a function of wavelength. (a) A typical solar irradiance spectrum output from FISM-M. (b) Irradiance converted to differential photon flux. (c) CO_2 photoionization cross sections from *Huebner and Mukherjee* [2015]. When multiplied together, Figures A1b and A1c result in the (d) differential ionization frequency, which is integrated over wavelength to provide total ionization frequency, as shown in several figures in this paper.

Appendix A: CO_2 Photoionization Rate

In this study we investigate the dependence of photochemical escape fluxes on the Sun's ability to ionize molecules in the upper atmosphere of Mars. However, it is important to choose an appropriate metric for this ability. Solar F10.7 radio emission measured on Earth has been used for several decades as a proxy for the EUV irradiance which causes this ionization [*Girazian and Withers*, 2015; *Hinteregger*, 1981]. For Mars, both F10.7 and directly measured EUV irradiance (from Earth orbit) in prominent ionizing lines (such as the 30.4 nm He-II emission), scaled and rotated from Earth to Mars, have been used to study the effects of photoionization [*Lillis et al*., 2010; *Withers*, 2009]. EUV irradiance at Mars is measured by the MAVEN Extreme Ultraviolet Monitor in three key wavelength ranges [*Eparvier et al*., 2015]. These measurements, plus full-spectrum measurements from Earth, are used to drive an empirical model of EUV and FUV spectral irradiance at Mars, called the Flare Irradiance Special Model for Mars (FISM-M) [*Thiemann et al*., 2017], which we take as the best estimate for this irradiance. An example of the output of FISM-M is shown in Figure A1.

However, to derive the most appropriate metric for solar radiation's ability to produce O_2^+ ions, we must convolve this irradiance spectrum with the photoionization cross section for CO_2 (since CO_2^+ is by far the dominant source of O_2^+ via the reaction $CO_2^+ + O \rightarrow CO + O_2^+$). This convolution is shown in Figures A1b–A1d, whereby differential photon flux (Figure A1b) is multiplied by photoionization cross section (Figure A1c), to arrive at differential ionization frequency (Figure A1d). We integrate this

differential ionization frequency with respect to wavelength to get total ionization frequency, which is the metric used throughout this manuscript.

Acknowledgments
The work of all US-based coauthors was supported by the MAVEN project. All data used in this study are publicly available at both the MAVEN Science Data Center (https://lasp.colorado.edu/maven/sdc/public/) and the Planetary Data System (http://atmos.nmsu.edu/data_and_services/atmospheres_data/MAVEN/maven_main.html). We would also like to thank the efforts of two anonymous reviewers for improving the paper substantially.

References

Andersson, L., R. E. Ergun, G. Delory, A. I. Eriksson, J. Westfall, H. Reed, J. F. McCauly, D. J. Summers, and D. Meyers (2015), The langmuir probe and waves experiment for MAVEN, *Space Sci. Rev.*, *195*, 173–198.

Andrews, D. J., L. Andersson, G. T. Delory, R. E. Ergun, A. I. Eriksson, C. M. Fowler, T. McEnulty, M. W. Morooka, T. Weber, and B. M. Jakosky (2015), Ionospheric plasma density variations observed at Mars by MAVEN/LPW, *Geophys. Res. Lett.*, *42*, 8862–8869, doi:10.1002/2015GL065241.

Ayres, T. R. (1997), Evolution of the solar ionizing flux, *J. Geophys. Res.*, *102*, 1641–1651, doi:10.1029/96JE03306.

Balakrishnan, N., V. Kharchenko, and A. Dalgarno (1998), Quantum mechanical and semiclassical studies of $N + N_2$ collisions and their application to thermalization of fast N atoms, *J. Chem. Phys.*, *108*, 943, doi:10.1063/1.475458.

Benna, M., P. R. Mahaffy, J. M. Grebowsky, J. L. Fox, R. V. Yelle, and B. M. Jakosky (2015), First measurements of composition and dynamics of the Martian ionosphere by MAVEN's Neutral Gas and Ion Mass Spectrometer, *Geophys. Res. Lett.*, *42*, 8958–8965, doi:10.1002/2015GL066146.

Bougher, S. W., S. Engel, R. G. Roble, and B. Foster (1999), Comparative terrestrial planet thermospheres 2. Solar cycle variation of global structure and winds at equinox, *J. Geophys. Res.*, *104*, 16,591–16,611, doi:10.1029/1998JE001019.

Bougher, S. W., S. Engel, R. G. Roble, and B. Foster (2000), Comparative terrestrial planet thermospheres 3. Solar cycle variation of global structure and winds at solstices, *J. Geophys. Res.*, *105*, 17,669–17,692, doi:10.1029/1999JE001232.

Brain, D. A., S. Barabash, S. Bougher, F. Duru, B. Jakosky, and R. Modolo (2017), Solar wind interaction and atmospheric escape, in *The Mars 6 Atmosphere*, edited by B. Haberle et al., Cambridge Univ. Press, Cambridge, doi:10.1017/9781139060172.

Chaufray, J. Y., R. Modolo, F. Leblanc, G. Chanteur, R. E. Johnson, and J. G. Luhmann (2007), Mars solar wind interaction: Formation of the Martian corona and atmospheric loss to space, *J. Geophys. Res.*, *112*, E09009, doi:10.1029/2007JE002915.

Cipriani, F., F. Leblanc, and J. J. Berthelier (2007), Martian corona: Nonthermal sources of hot heavy species, *J. Geophys. Res.*, *112*, E07001, doi:10.1029/2006JE002818.

Cravens, T. E., et al. (2016), Hot oxygen escape from Mars: Simple scaling with solar EUV irradiance, *J. Geophys. Res. Space Physics*, *122*, 1102–1116, doi:10.1002/2016JA023461.

Deighan, J., et al. (2015), MAVEN IUVS observation of the hot oxygen corona at Mars, *Geophys. Res. Lett.*, *42*, 9009–9014, doi:10.1002/2015GL065487.

England, S. L., et al. (2016), Simultaneous observations of atmospheric tides from combined in situ and remote observations at Mars from the MAVEN spacecraft, *J. Geophys. Res. Planets*, *121*, 594–607, doi:10.1002/2016JE004997.

Eparvier, F., P. C. Chamberlin, and T. N. Woods (2015), The Solar Extreme Ultraviolet Monitor for MAVEN, *Space Sci. Rev.*, *195*(1–4), 293–301, doi:10.1007/s11214-015-0195-2.

Ergun, R. E., M. W. Morooka, C. M. Fowler, G. Delory, D. J. Andrews, A. I. Eriksson, T. McEnulty, and B. Jakosky (2015), Dayside electron temperature and density profiles at Mars: First results from the MAVEN LPW instrument, *Geophys. Res. Lett.*, *42*, 8846–8853, doi:10.1002/2015GL065280.

Ergun, R. E., et al. (2016), Enhanced O_2^+ loss at Mars due to an ambipolar electric field from electron heating, *J. Geophys. Res. Space Physics*, *121*, 4668–4678, doi:10.1002/2016JA022349.

Fillingim, M. O., R. J. Lillis, S. L. England, L. M. Peticolas, D. A. Brain, J. S. Halekas, C. Paty, D. Lummerzheim, and S. W. Bougher (2012), On wind-driven electrojets at magnetic cusps in the nightside ionosphere of Mars, *Earth Planets Space*, *64*(2), 93–103, doi:10.5047/eps.2011.04.010.

Fowler, C. M., et al. (2015), The first in situ electron temperature and density measurements of the Martian nightside ionosphere, *Geophys. Res. Lett.*, *42*, 8854–8861, doi:10.1002/2015GL065267.

Fox, J. L., and A. B. Hać (2009), Photochemical escape of oxygen from Mars: A comparison of the exobase approximation to a Monte Carlo method, *Icarus*, *204*(2), 527–544, doi:10.1016/j.icarus.2009.07.005.

Fox, J. L., and A. B. Hac (2014), The escape of O from Mars: Sensitivity to the elastic cross sections, *Icarus*, *228*, 375–385, doi:10.1016/j.icarus.2013.10.014.

Girazian, Z., and P. Withers (2015), An empirical model of the extreme ultraviolet solar spectrum as a function of F10.7, *J. Geophys. Res. Space Physics*, *120*, 6779–6794, doi:10.1002/2015JA021436.

Gonzalez-Galindo, F., J. Y. Chaufray, M. A. Lopez-Valverde, G. Gilli, F. Forget, F. Leblanc, R. Modolo, S. Hess, and M. Yagi (2013), Three-dimensional Martian ionosphere model: I. The photochemical ionosphere below 180 km, *J. Geophys. Res. Planets*, *118*, 2105–2123, doi:10.1002/Jgre.20150.

Groller, H., H. Lichtenegger, H. Lammer, and V. I. Shematovich (2014), Hot oxygen and carbon escape from the martian atmosphere, *Planet. Space Sci.*, *98*, 93–105, doi:10.1016/j.pss.2014.01.007.

Halekas, J. S., E. R. Taylor, G. Dalton, G. Johnson, D. W. Curtis, J. P. McFadden, D. L. Mitchell, R. P. Lin, and B. M. Jakosky (2015), The MAVEN solar wind ion analyzer, *Space Sci. Rev.*, *195*(1), 125–151, doi:10.1007/s11214-013-0029-z.

Hanson, W. B., S. Sanatani, and D. Zuccaro (1976), Retarding potential analyzer measurements from Viking Landers, *Trans. AGU*, *57*(12), 966–966.

Hanson, W. B., S. Sanatani, and D. R. Zuccaro (1977), The Martian ionosphere as observed by the Viking retarding potential analyzers, *J. Geophys. Res.*, *82*, 4351–4363, doi:10.1029/JS082i028p04351.

Hinteregger, H. E. (1981), Representations of solar EUV fluxes for aeronomical applications, *Adv. Space Res.*, *1*, 39–52, doi:10.1016/0273-1177(81)90416-6.

Hodges, R. R. (2002), The rate of loss of water from Mars, *Geophys. Res. Lett.*, *29*(3), 1038, doi:10.1029/2001GL013853.

Huebner, W. F., and J. Mukherjee (2015), Photoionization and photodissociation rates in solar and blackbody radiation fields, *Planet. Space Sci.*, *106*, 11–45, doi:10.1016/j.pss.2014.11.022.

Jakosky, B. M., et al. (2014), The Mars Atmosphere and Volatile Evolution (MAVEN) mission, *Space Sci. Rev.*, doi:10.1007/s11214-015-0139-x.

Johnstone, C. P., M. Güdel, I. Brott, and T. Lüftinger (2015), Stellar winds on the main-sequence. II. The evolution of rotation and winds, *Astron. Astrophys.*, *577*, 22, doi:10.1051/0004-6361/201424550.

Keating, G. M., et al. (1998), The structure of the upper atmosphere of Mars: In situ accelerometer measurements from Mars global surveyor, *Science*, *279*(5357), 1672–1676, doi:10.1126/science.279.5357.1672.

Kharchenko, V., A. Dalgarno, B. Zygelman, and J. H. Yee (2000), Energy transfer in collisions of oxygen atoms in the terrestrial atmosphere, *J. Geophys. Res.*, *105*, 24,899–24,906, doi:10.1029/2000JA000085.

Kim, J., A. F. Nagy, J. L. Fox, and T. E. Cravens (1998), Solar cycle variability of hot oxygen atoms at Mars, *J. Geophys. Res.*, *103*, 29,339–29,342, doi:10.1029/98JA02727.

Krestyanikova, M. A., and V. I. Shematovich (2005), Stochastic models of hot planetary and satellite coronas: A photochemical source of hot oxygen in the upper atmosphere of Mars, *Sol. Syst. Res.*, *39*(1), 22–32, doi:10.1007/s11208-005-0002-9.

Lammer, H., J. F. Kasting, E. Chassefiere, R. E. Johnson, Y. N. Kulikov, and F. Tian (2008), Atmospheric escape and evolution of terrestrial planets and satellites, *Space Sci. Rev.*, *139*(1), 399–436, doi:10.1007/978-0-387-87825-6_11.

Larson, D., et al. (2015), The MAVEN solar energetic particle investigation, *Space Sci. Rev.*, *195*, 153–172, doi:10.1007/s11214-015-0218-z.

Lee, Y., M. R. Combi, V. Tenishev, S. W. Bougher, J. Deighan, N. M. Schneider, W. E. McClintock, and B. M. Jakosky (2015a), A comparison of 3-D model predictions of Mars' oxygen corona with early MAVEN IUVS observations, *Geophys. Res. Lett.*, *42*, 9015–9022, doi:10.1002/2015GL065291.

Lee, Y., M. R. Combi, V. Tenishev, S. W. Bougher, and R. J. Lillis (2015b), Hot oxygen corona at Mars and the photochemical escape of oxygen: Improved description of the thermosphere, ionosphere, and exosphere, *J. Geophys. Res. Planets*, *120*, 1880–1892, doi:10.1002/2015JE004890.

Lillis, R. J., and D. A. Brain (2013), Nightside electron precipitation at Mars: Geographic variability and dependence on solar wind conditions, *J. Geophys. Res. Space Physics*, *118*, 3546–3556, doi:10.1002/Jgra.50171.

Lillis, R. J., D. L. Mitchell, R. P. Lin, and M. H. Acuna (2008), Electron reflectometry in the Martian atmosphere, *Icarus*, *194*(2), 544–561, doi:10.1016/j.icarus.2007.09.030.

Lillis, R. J., D. A. Brain, S. L. England, P. Withers, M. O. Fillingim, and A. Safaeinili (2010), Total electron content in the Mars ionosphere: Temporal studies and dependence on solar EUV flux, *J. Geophys. Res.*, *115*, A11314, doi:10.1029/2010JA015698.

Lillis, R. J., M. O. Fillingim, and D. A. Brain (2011), Three-dimensional structure of the Martian nightside ionosphere: Predicted rates of impact ionization from Mars Global Surveyor Magnetometer and Electron Reflectometer measurements of precipitating electrons, *J. Geophys. Res.*, *116*, A12317, doi:10.1029/2011JA016982.

Lillis, R. J., et al. (2015), Characterizing atmospheric escape from mars today and through time, with MAVEN, *Space Sci. Rev.*, *195*, 357–422, doi:10.1007/s11214-015-0165-8.

Mahaffy, P. R., et al. (2014), The Neutral Gas and Ion Mass Spectrometer on the Mars atmosphere and volatile evolution mission, *Space Sci. Rev.*, *195*(1), 49–73, doi:10.1007/s11214-014-0091-1.

Mahaffy, P. R., M. Benna, M. Elrod, R. V. Yelle, S. W. Bougher, S. W. Stone, and B. M. Jakosky (2015), Structure and composition of the neutral upper atmosphere of Mars from the MAVEN NGIMS investigation, *Geophys. Res. Lett.*, *42*, 8951–8957, doi:10.1002/2015GL065329.

McClintock, W., N. M. Schneider, G. M. Holsclaw, J. Clarke, A. Hoskins, I. Stewart, F. Montmessin, and R. Yelle (2015), The imaging ultraviolet spectrograph for the MAVEN mission, *Space Sci. Rev.*, *195*(1–4), 75–124, doi:10.1007/s11214-014-0098-7.

McFadden, J., et al. (2015), The MAVEN Suprathermal and thermal Ion Composition (STATIC) instrument, *Space Sci. Rev.*, doi:10.1007/s11214-015-0175-6.

Medvedev, A. S., and E. Yigit (2012), Thermal effects of internal gravity waves in the Martian upper atmosphere, *Geophys. Res. Lett.*, *39*, L05201, doi:10.1029/2012GL050852.

Morgan, D. D., D. A. Gurnett, D. L. Kirchner, J. L. Fox, E. Nielsen, and J. J. Plaut (2008), Variation of the Martian ionospheric electron density from Mars Express radar soundings, *J. Geophys. Res.*, *113*, A09303, doi:10.1029/2008JA013313.

Morschhauser, A., V. Lesur, and M. Grott (2014), A spherical harmonic model of the lithospheric magnetic field of Mars, *J. Geophys. Res. Planets*, *119*, 1162–1188, doi:10.1002/2013JE004555.

Nagy, A. F., M. W. Liemohn, J. L. Fox, and J. Kim (2001), Hot carbon densities in the exosphere of Mars, *J. Geophys. Res.*, *106*, 21,565–21,568, doi:10.1029/2001JA000007.

Němec, F., D. D. Morgan, D. A. Gurnett, and D. A. Brain (2011), Areas of enhanced ionization in the deep nightside ionosphere of Mars, *J. Geophys. Res.*, *116*, E06006m, doi:10.1029/2011JE003804.

Nier, A. O., W. B. Hanson, A. Seiff, M. B. Mcelroy, N. W. Spencer, R. J. Duckett, T. C. D. Knight, and W. S. Cook (1976), Composition and structure of martian atmosphere—Preliminary results from Viking-1, *Science*, *193*(4255), 786–788, doi:10.1126/science.193.4255.786.

Petrignani, A., F. Hellberg, R. D. Thomas, M. Larsson, P. C. Cosby, and W. J. van der Zande (2005), Electron energy-dependent product state distributions in the dissociative recombination of O_2^+, *J. Chem. Phys.*, *122*(23), 234311, doi:10.1063/1.1937388.

Rahmati, A., D. E. Larson, T. E. Cravens, R. J. Lillis, P. A. Dunn, J. S. Halekas, J. E. Connerney, F. G. Eparvier, E. M. B. Thiemann, and B. M. Jakosky (2015), MAVEN insights into oxygen pickup ions at Mars, *Geophys. Res. Lett.*, *42*, 8870–8876, doi:10.1002/2015GL065262.

Rahmati, A., et al. (2017), MAVEN measured oxygen and hydrogen pickup ions: Probing the Martian exosphere and neutral escape, *J. Geophys. Res. Space Physics*, *122*, doi:10.1002/2016JA023371.

Ribas, I., E. F. Guinan, M. Güdel, and M. Audard (2005), Evolution of the solar activity over time and effects on planetary atmospheres. I. High-energy irradiances (1–1700 Å), *Astrophys. J.*, *622*(1), 680, doi:10.1086/427977.

Riousset, J. A., C. S. Paty, R. J. Lillis, M. O. Fillingim, S. L. England, P. G. Withers, and J. P. M. Hale (2013), Three-dimensional multifluid modeling of atmospheric electrodynamics in Mars' dynamo region, *J. Geophys. Res. Space Physics*, *118*, 3647–3659, doi:10.1002/Jgra.50328.

Schunk, R. W., and A. Nagy (2000), *Ionospheres: Physics, Plasma Physics, and Chemistry*, Cambridge Univ. Press, New York.

Thiemann, E. M. B., P. C. Chamberlin, F. G. Eparvier, B. Templeman, T. N. Woods, S. W. Bougher, and B. M. Jakosky (2017), The MAVEN EUVM model of solar spectral irradiance variability at Mars: Algorithms and results, *J. Geophys. Res. Space Physics*, *122*, doi:10.1002/2016JA023512.

Tu, L., C. P. Johnstone, M. Güdel, and H. Lammer (2015), The extreme ultraviolet and X-ray Sun in rime: High-energy evolutionary tracks of a solar-like star, *A&A*, *577*, doi:10.1051/0004-6361/201526146.

Valeille, A., M. R. Combi, S. W. Bougher, V. Tenishev, and A. F. Nagy (2009a), Three-dimensional study of Mars upper thermosphere/ionosphere and hot oxygen corona: 2. Solar cycle, seasonal variations, and evolution over history, *J. Geophys. Res.*, *114*, E11006, doi:10.1029/2009JE003389.

Valeille, A., V. Tenishev, S. W. Bougher, M. R. Combi, and A. F. Nagy (2009b), Three-dimensional study of Mars upper thermosphere/ionosphere and hot oxygen corona: 1. General description and results at equinox for solar low conditions, *J. Geophys. Res.*, *114*, E11005, doi:10.1029/2009JE003388.

Valeille, A., M. R. Combi, V. Tenishev, S. W. Bougher, and A. F. Nagy (2010), A study of suprathermal oxygen atoms in Mars upper thermosphere and exosphere over the range of limiting conditions, *Icarus*, *206*(1), 18–27, doi:10.1016/j.icarus.2008.08.018.

Withers, P. (2009), A review of observed variability in the dayside ionosphere of Mars, *Adv. Space Res.*, *44*(3), 277–307, doi:10.1016/j.asr.2009.04.027.

Wright, C. J. (2012), A one-year seasonal analysis of martian gravity waves using MCS data, *Icarus*, *219*(1), 274–282, doi:10.1016/j.icarus.2012.03.004.

Zhao, J., and F. Tian (2015), Photochemical escape of oxygen from early Mars, *Icarus*, *250*, 477–481, doi:10.1016/j.icarus.2014.12.032.